Influence of grain growth on CO2 ice spectroscopic profiles : Modelling for dense cores and disk

Emmanuel Dartois, Jennifer A. Noble, Nathalie Ysard, Karine Demyk, Marin Chabot

To cite this version:

Emmanuel Dartois, Jennifer A. Noble, Nathalie Ysard, Karine Demyk, Marin Chabot. Influence of grain growth on CO2 ice spectroscopic profiles : Modelling for dense cores and disk. Astronomy and Astrophysics - A&A, 2022, 666, pp.A153. 10.1051/0004-6361/202243929 . hal-03875246

A&A 666, A153 (2022)
https://doi.org/10.1051/0004-6361/202243929

Astronomy & Astrophysics

Influence of grain growth on CO_2 ice spectroscopic profiles

Modelling for dense cores and disks

E. Dartois[1], J. A. Noble[2], N. Ysard[3], K. Demyk[4], and M. Chabot[5]

[1] Institut des Sciences Moléculaires d'Orsay, UMR8214, CNRS, Université Paris-Saclay, 91405 Orsay, France
e-mail: `emmanuel.dartois@universite-paris-saclay.fr`
[2] CNRS, Aix-Marseille Université, Laboratoire PIIM, Marseille, France
[3] Institut d'Astrophysique Spatiale, CNRS, Université Paris-Saclay, Bât. 121, 91405 Orsay Cedex, France
[4] IRAP, Université de Toulouse, CNRS, UPS, IRAP, 9 Av. colonel Roche, BP 44346, 31028 Toulouse Cedex 4, France
[5] Laboratoire de physique des deux infinis Irène Joliot-Curie, CNRS-IN2P3, Université Paris-Saclay, 91405 Orsay, France

Received 3 May 2022 / Accepted 21 July 2022

ABSTRACT

Context. Interstellar dust grain growth in dense clouds and protoplanetary disks, even when moderate, affects the observed interstellar ice profiles as soon as a significant fraction of dust grains are in the size range close to the wave vector at the considered wavelength. The continuum baseline correction made prior to analysing ice profiles influences the subsequent analysis and hence the estimated ice composition, which are typically obtained by band fitting using thin film ice mixture spectra.

Aims. We explore the effect of grain growth on the spectroscopic profiles of ice mantle constituents, focusing particularly on carbon dioxide, with the aim of understanding how it can affect interstellar ice mantle spectral analysis and interpretation.

Methods. Using the discrete dipole approximation for scattering and absorption of light, the mass absorption coefficients of several distributions of grains – composed of ellipsoidal silicate cores with water and carbon dioxide ice mantles – are calculated. A few models also include amorphous carbon in the core and pure carbon monoxide in the ice mantle. We explore the evolution of the size distribution starting in the dense core phase in order to simulate the first steps of grain growth up to three microns in size. The resulting mass absorption coefficients are injected into RADMC-3D radiative transfer models of spherical dense core and protoplanetary disk templates to retrieve the observable spectral energy distributions. Calculations are performed using the full scattering capabilities of the radiative transfer code. We then focus on the particularly relevant calculated profile of the carbon dioxide ice band at 4.27 µm.

Results. The carbon dioxide anti-symmetric stretching mode profile is a meaningful indicator of grain growth. The observed profiles towards dense cores obtained with the Infrared Space Observatory and Akari satellites already show profiles possibly indicative of moderate grain growth.

Conclusions. The observation of true protoplanetary disks at high inclination with the *James Webb* Space Telescope should present distorted profiles that will allow constraints to be placed on the extent of dust growth. The more evolved the dust size distribution, the more the extraction of the ice mantle composition will require both understanding and taking grain growth into account.

Key words. ISM: lines and bands – dust, extinction – radiative transfer – protoplanetary disks – ISM: clouds – infrared: ISM

1. Introduction

In the first stages of star formation, protostars are still embedded in their parental cloud, where an active gas-grain chemistry is at work. Using either (i) background stars for dense clouds or (ii) a nascent protostellar object once it is able to emit sufficient light flux in the vibrational infrared wavelength range, or in a few protoplanetary disks well inclined towards the observer, the infrared pencil beam allows the probing of the composition of the cloud or circumstellar dust. The low-temperature ice mantles formed on top of or mixed with refractory dust (silicates and/or organics) can be retrieved. A harvest of astronomical observations from ground-based telescopes (e.g. UKIRT, IRTF, CFHT, and VLT) or satellites (e.g. IRAS, ISO, Akari, and *Spitzer*) of such lines of sight has led, since the late seventies, to the deciphering of the chemical compositions, column densities, and variations associated with these ice mantles (e.g. Boogert et al. 2008, 2015; Öberg et al. 2011; Dartois 2005; van Dishoeck 2004; Gibb et al. 2004; Keane et al. 2001; Dartois et al. 1999b; Brooke et al. 1999, and references therein). The interpretation of these observed spectra is mainly based on their comparison with the infrared spectra of laboratory-produced ice films of well-controlled composition and cryogenic temperatures (e.g. Hudson et al. 2014, 2021; Palumbo et al. 2020; Rachid et al. 2020; Terwisscha van Scheltinga et al. 2018; Öberg et al. 2007; Dartois et al. 2003, 1999a,b; Moore & Hudson 1998; Ehrenfreund et al. 1997; Gerakines et al. 1995; Hudgins et al. 1993). The routes investigated are the influence of the ice mixture on the line width and position, temperature modifications, segregation (phase separation), and/or intermolecular interactions (polar or apolar ices and molecular complexes). The impact of a distribution of grain shapes, mainly in the Rayleigh regime, is also explored in some cases. The literature is dominated by analyses based on the decomposition of the observed astronomical profiles into principal components from different ice mixtures. When dust grains evolve from the diffuse interstellar medium (ISM) to the dense phase and the protoplanetary phases, grains grow. This will affect the observed profiles and is expected to be, at least partly, responsible for enhanced scattering effects in dense cloud evolution, often referred to as cloudshine or coreshine effects (Ysard et al. 2016, 2018; Saajasto et al. 2018; Jones et al. 2016; Steinacker et al. 2015; Lefèvre et al. 2014). The growth can also be inferred from the evolution of the silicate-to-K band ratio ($\tau_{9.7}/A_K$; e.g. Madden et al. 2022; van Breemen et al. 2011; Chiar et al. 2007).

This is already evidenced from direct spectroscopic profile evolutions for silicates observed in emission coming from the surface of some disks (e.g. van Boekel et al. 2005; Meeus 2011). Grain growth is important, but so is the depletion of the smallest grains in the distribution. Grain growth is a parameter that will take on an increasing importance for the interpretation of observed ice mantle band profiles, especially in the study of protoplanetary disks (Tazaki et al. 2021a,b; Terada & Tokunaga 2017; Terada et al. 2007; Honda et al. 2009).

The inventory of solid-state material sometimes combines ice feature investigation with radiative transfer codes to simulate the observed spectral energy distribution and/or chemical models (e.g. Pontoppidan et al. 2005; Ballering et al. 2021). The ice band spectroscopic profiles observed at medium to high spectral resolution intrinsically contain information that can be used to constrain the extent of grain growth since they are affected by this growth. Carbon dioxide displays several characteristics that are particularly interesting for probing grain growth. It is one of the main and ubiquitous ice mantle constituents, along with water and, depending on the line of sight, carbon monoxide. The carbon dioxide stretching mode around 4.27 µm possesses a fairly narrow absorption band with a typical full width at half maximum (FWHM) of tens of cm^{-1}, depending on the exact ice mixture environment (e.g. Ehrenfreund et al. 1996, 1999), whereas the water ice FWHM is several hundred cm^{-1}. In addition to the relatively high contrast expected in the CO_2 ice profile due its narrowness, carbon dioxide absorbs in a relatively clean region of the infrared spectrum. For the absorption band of water ice centred at 3.1 µm, the red wing of the profile is modified not only by grain growth but also by additional absorption from, for example, methanol and the 3.47 µm band assigned to the presence of ammonia in the water mantle. The carbon monoxide stretching mode, lying at slightly higher wavelengths than that of carbon dioxide, is also in a relatively clean region. Some sources show a significant absorption at 4.62 µm, attributed to the presence of OCN^-, that can mainly affect the blue side of the CO absorption profile. It has been investigated and discussed in Dartois (2006), where it was shown that grain growth to micron sizes can still produce an observed large red component in its absorption profiles towards some lines of sight. Some young stellar object (YSO) spectra can also harbour hydrogen lines in emission, such as Pfund β (4.654 µm) and Brackett α (4.051 µm), which has to be taken into account. Their contribution can either be estimated from the set of observed hydrogen lines and/or taken out of the profile analysis if significant for spectra with high enough spectral resolution given their narrow profile widths. The integrated absorption cross-section of the carbon dioxide band is relatively high, higher than carbon monoxide, an additional factor that makes it a good target for investigating how grain growth affects spectroscopic band profiles.

This article is dedicated to the prediction of the CO_2 ice mantle spectral profile behaviour expected for grain size distributions that have evolved, starting from the diffuse ISM. We describe in Sect. 2 the ice mixtures and optical constant calculations used to build the ice mantle models. We discuss in Sect. 3 the dust grain shapes adopted to represent the diversity of shapes in the distribution, and in Sect. 4 the discrete dipole approximation (DDA) method for evaluating the absorption and scattering matrices for these grains. We apply the method to evolved dust grain size distributions resulting from previous literature models in Sect. 5. In Sect. 6, a Monte Carlo radiative transfer code (RADMC-3D) is used to calculate the emerging spectra from spherical dust clouds and a protoplanetary disk observed at various inclination angles along the line of sight, with a particular focus on the evolution of the CO_2 ice stretching band. Finally, in Sect. 7 we draw conclusions on the interpretation of principal component analysis of ice profiles and make predictions on grain growth constraints in the perspective of *James Webb* Space Telescope (JWST) observations.

2. Experiments and methods

In order to build spectroscopic profiles of ice mantles, the first modelling ingredients to define are interstellar relevant ice mixtures, as recorded in the laboratory, and deriving their optical constants. Then appropriate dust grains shape and size distributions are adopted and their absorption and scattering properties calculated. These steps are described below.

2.1. Ice mixture and optical constant calculations

We use two binary water and carbon dioxide ice mixtures to explore the effect of a moderate to high CO_2 ice proportion. These mixtures, called M15 and M50 are CO_2/H_2O low-temperature amorphous mixed ices, with a carbon dioxide to water content of 15% and 50%, respectively. These values cover the CO_2 range observed towards most lines of sight, with 15% being the closer to massive YSOs or comets (e.g. Fig. 8 Boogert et al. 2015), whereas a higher CO_2 fraction can be observed towards low mass YSOs and 50% represents a possible, unusually CO_2-rich, mixture.

The set of ice optical constants used is built from ice film laboratory experiments; a co-deposited CO_2/H_2O mixture measured in the near to mid-infrared in our laboratory for the high CO_2 mixture 50% (M50), while the CO_2/H_2O 15% ice mixture (M15) is from Ehrenfreund et al. (1996). Far-infrared water ice optical constants adopted are from Trotta (1996). The millimetre and UV to visible optical constants are interpolated from pure H_2O ice literature data (Warren 1984). Real measurements for the same CO_2/H_2O mixtures over the full range would be, of course, better but are not available. Such an extension will, however, have little influence on the calculated profiles in the near to mid-infrared range, where the correct optical constants for the mixed ices are used. They are extrapolated outside this range in order to implement them into the radiative transfer model used in the final step of the analysis. The scale of the imaginary part (k) of the complex refractive index is validated using

$$A = \int_{\mathrm{band}} 4\pi k(\bar{\nu}) \mathrm{d}\bar{\nu} M/(N_{\mathrm{A}}\rho), \tag{1}$$

where A is the integrated band strength ($cm\,mol^{-1}$), M the molar mass, N_A the Avogadro number and ρ the density of the ice, by checking that it falls within the range of expected band strengths. In the M15 mixture, the estimated water ice stretching mode band strength is about 1.9×10^{-16} $cm\,mol^{-1}$, whereas for the M50 mixture it is about 1.6×10^{-16} $cm\,mol^{-1}$, in agreement with what is expected (e.g. Fig. 4 of Öberg et al. 2007). Self-consistency for the real and imaginary components of the optical constants is ensured by calculating the refractive index from a Kramers–Kronig transformation of the imaginary part of the complex index, re-scaled to the visible real part of the index assumed to be 1.3, a typical value for H_2O ice, and also close to that of many ices of astrophysical interest (Trotta 1996; Satorre et al. 2008).

The real part of the complex refractive index, n, is calculated using the Kramers–Kronig integral dispersion relation, related to the imaginary part k by

$$n(\bar{\nu}) = n(\infty) + \frac{2}{\pi}\int_0^{\infty} \frac{\bar{x}\;k(\bar{x})}{\bar{x}^2 - \bar{\nu}^2}\mathrm{d}\bar{x}. \tag{2}$$

To numerically calculate n over a finite frequency interval $\{\bar{\nu}_{\min}; \bar{\nu}_{\max}\}$, the subtractive Kramers–Kronig relation is preferred:

$$n(\bar{\nu}) = n(\bar{\nu}_0) + \frac{2}{\pi}\int_{\bar{\nu}_{\min}}^{\bar{\nu}_{\max}} \left(\frac{\bar{x}k(\bar{x}) - \bar{\nu}k(\bar{\nu})}{\bar{x}^2 - \bar{\nu}^2} - \frac{\bar{x}k(\bar{x}) - \bar{\nu}_0 k(\bar{\nu}_0)}{\bar{x}^2 - \bar{\nu}_0^2}\right)\mathrm{d}\bar{x}, \tag{3}$$

using the anchor point at frequency $\bar{\nu}_0$, away from strong absorptions, with a known value $n(\bar{\nu}_0)$. For ices, generally, as stated above, a value in the visible domain where most of them do not absorb significantly, is adopted. Our spectra used in the optical constant derivation were recorded in transmittance at normal or close to normal incidence. In the absence of a dedicated experiment to record simultaneously the refractive index, the infrared spectrum and the ice density, and an experiment designed specifically for a complete optical constants inversion process, the absolute values of k will vary slightly with the refractive index and scale with the density values. Uncertainties for the derived optical constants in the main mid-infrared bands, the core of the analysis in this article, are conservatively estimated to be below 20%.

The refractory material is assumed to be represented by the so-called astronomical silicates optical constants from Draine & Lee (1984). The adopted pure silicate cores and one ice mixture for each model is a simplification over all the possible ice mixtures and core compositions. This consideration was made based on main components, and to avoid mixing the effect of too many parameters in the resulting comparisons. In order to compensate for this potential oversimplification, we expand our test set with two additional models. One includes a possible additional pure carbon monoxide component in the ice mantle as, towards some lines of sight, at high visual extinction the condensation of pure CO onto the mantle has been observed (e.g. Pontoppidan 2006; i.e. CO not mixed with the other components in the ice mantle). For this model we take the optical constants from Palumbo et al. (2006). The interstellar dust distribution in the ISM comprises siliceous and carbonaceous components. We thus also explore a model with a possible refractory core mixture including amorphous carbon with optical constants taken from Rouleau & Martin (1991). The optical constants calculated and used in the models are shown in Fig. 1.

2.2. Dust grain shape distribution

The exact shape distribution of interstellar grains is not known, but from polarisation considerations is known not to be represented adequately by pure spheres. To sample the expected diversity, several shape distributions may be adopted (e.g. Fabian et al. 2001; Min et al. 2003). Among the most convenient shapes are ellipsoids for their mathematical properties, as discussed in, for example, Draine & Hensley (2021). In the possible continuous distributions of ellipsoidal (under the name of CDE or CDE1) shapes, one of the most popular is the uniform weighting, where any shape has an equal probability of occurring. With such a weighting scheme, extreme shapes that have a non-physical probability of being present in space, such as when the ellipsoid tends to be like an infinite rod or to be planar, have the same weight as more compact or spheroidal shapes. This is unrealistic and has led to the adoption of a quadratic weighting scheme used in, for example, Draine & Hensley (2021), Dartois (2006), Fabian et al. (2001), and Ossenkopf et al. (1992) under the name of quadratic continuous distribution of ellipsoids (QCDE) or CDE2. This distribution explores a variety of ellipsoidal shapes, but with such a weighting scheme, due to the interdependence of geometrical factors, that if one axis of the ellipsoid is far from the others its occurrence, and thus contribution to the distribution, drops. An ellipsoid with axis ratios commensurate to 5:1:1 will have a probability of about 0.33 with respect to a sphere, and an ellipsoid commensurate to 100:1:1 (i.e. a needle) or 100:100:1 (i.e. a disk) would contribute as little as 0.0028 or 0.0011, respectively.

2.3. Ice distributions

We can consider three different scenarios of growth and acquirement of an ice mantle that will define the distribution of ices with respect to the refractory material in the grains (the representations of such models are shown in Fig. 2).

The simplest model (i) assumes the impact of molecules, atoms, and/or radicals on the initial ISM grain distribution builds the ice mantle from the gas phase. Therefore, the grain volume growth due to the ice mantle is given by

$$4\pi a^2 \dot{a} = \pi a^2 \sum_{i=1}^{N} n_i \;\frac{m_i}{\rho}\; v_i \; s_i, \tag{4}$$

where a is the grain radius, n_i and m_i are the density and mass of impinging molecules or nuclei with velocity v_i, ρ is the mass volume density of the accreting mantle, and s_i is an ‘efficiency factor’ that includes the sticking coefficient of the impactor, its reaction rate, and so on (the ratio $s_i\, m_\mathrm{i}/\rho$ is the volume increase per impact). Equation (4) shows that the grain radius growth $\dot{a}$ is independent of the grain radius. As a consequence, the acquired mantle thickness is constant on each grain size, and the ice to core volume ratio will be very high for the small grains and very low for the big grains in the distribution. Extending this to bigger grains when the upper size end of the distribution increases due to grain aggregation is equivalent to assuming that ice growth proceeds only after refractory core aggregation is fully completed. We do not model this distribution here, as it is probably the least physical among the growth properties. In addition we expect only mild spectral changes for the ice features with respect to the Mathis–Rumpl–Nordsieck (MRN) distribution (Mathis et al. 1977), as most of the ice volume is carried, within such an assumption, by the smallest grains (see e.g. Fig. 2 from Dartois 2006).

The second model (ii) assumes an ellipsoid refractory core coated by the ice mantle, ascribing each grain an individual constant Vice/Vcore ratio equivalent to the mean value observed. Such a model can be interpreted as the continuous aggregation of ice mantle on refractory grains accompanied by, if ices are mobile enough (e.g. upon energetic events), a progressive settling of the refractory core mainly inside the grain, ices migrating partly to the surface. This distribution is called the QCDE.

The final scenario (iii) is a stochastic sticking of the initial ISM dust grain distribution, each coated with an ice mantle, aggregating into a bigger grain. This distribution is called hereafter the compact stochastic distribution of ellipsoids (CSDE).

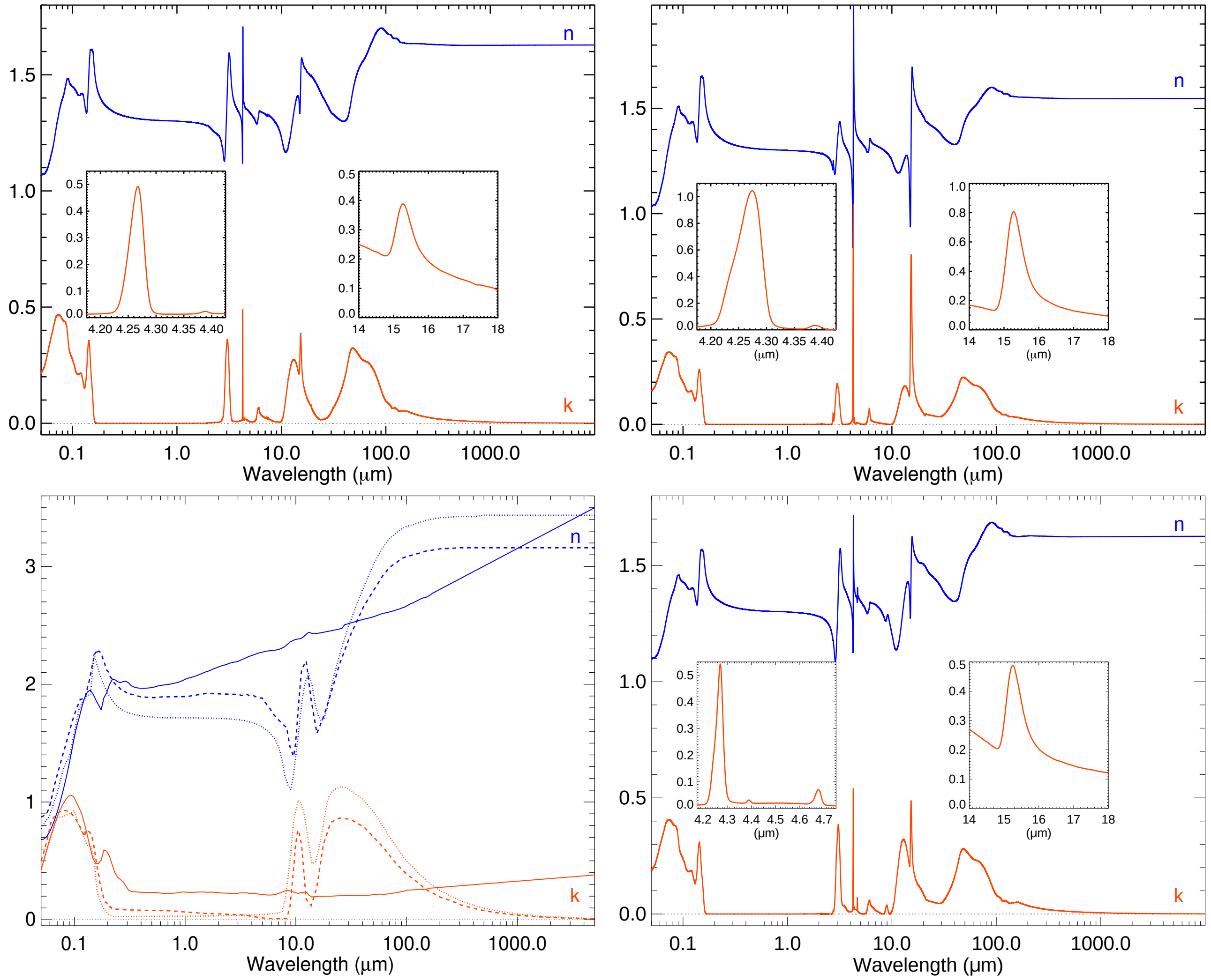

Fig. 1. Optical constants used in the models. *Upper left*: complex optical constants for the CO_2:H_2O 15:100 ice mixture (M15). Close-ups are shown for the imaginary part of the constant for the CO_2 stretching and bending modes. *Upper right*: complex optical constants for the CO_2:H_2O 50:100 ice mixture (M50). Close-ups are shown for the imaginary part of the constant for the CO_2 stretching and bending modes. *Lower left*: complex optical constants for the 'astrosilicates' (Draine & Lee 1984) and amorphous carbon AC1 from Rouleau & Martin (1991). *Lower right*: complex optical constants for the H_2O:CO_2:CO:NH3 100:16:8:8 ice mixture. Close-ups are shown for the imaginary part of the constant for the CO_2 and CO stretching modes and CO_2 bending mode. See text for details.

These differences in ice distributions will have consequences on the resulting ice spectral features. We consider only QCDE and CSDE in the following models.

2.4. Discrete dipole approximation calculations

To model an individual ice-mantle-coated refractory ellipsoid grain or mixed ice–refractory grains, we made use of the DDA program DDSCAT (version 7.3, Draine & Flatau 2013, 2008, 2000). The QCDE model calculations were performed with a scheme similar to that presented in the appendix of Dartois (2006), namely over all possible ellipsoids with relative non-degenerated integer aspect ratios of their three axes, between 1 and 5, with the first axis fixed to the highest integer. This provides 15 possibilities in total, which are shown in Fig. 3. The orientation average of the cross section for each ellipsoid, is performed over 16 angles equally sampling the relative orientation of individual ellipsoids with respect to the incoming plane wave. This calculation is performed over two incident orthogonal polarisations, then averaged over angles orientations, for grain sizes covering the range of our distributions (described in the following), sampled from 0.005 μm up to 3 μm (at 11 sizes). The number of dipoles used in the calculations is dependent on two parameters: the first one is the overall grain size, in order to set constraints on the code precision, and the second one is to satisfy enough accuracy of the modelled ice mantle to silicates core volume ratio. The number of dipoles for 0.005 μm grains is as low as 15 000, whereas above 0.5 μm it is up to 64 000. We calculate the absorption and scattering properties, as well as the Mueller scattering matrices for each ellipsoidal ice-coated grain, with an equivalent effective radius $a_{\rm eff}$, the radius of a sphere corresponding to the same volume corresponding to each grain size. Once these calculations have been made, they are used to build the mass absorption and scattering coefficient for a prescribed dust grain size distribution, which we discuss in the grain growth modelling section.

For the CSDE model we stochastically generate dipoles with the refractory or ice composition attribute in the volume of the desired shape, with relative proportions corresponding to their volume ratios, and proceed as for the QCDE model for the

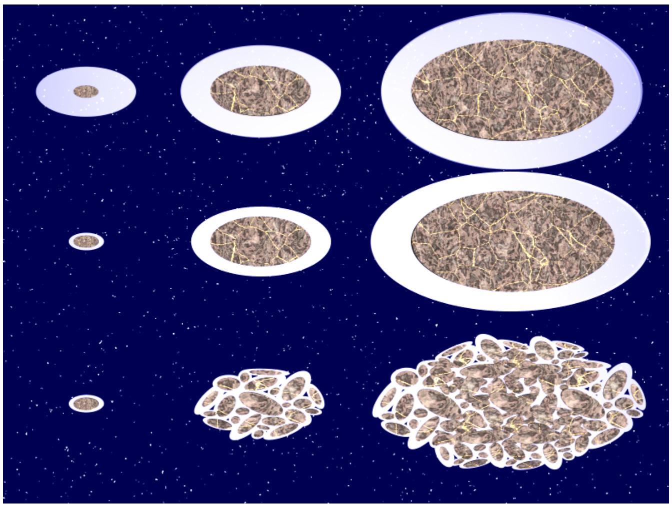

Fig. 2. Sketch of the different ice distributions with respect to refractory grains during grain growth addressed in the modelling: (i) constant ice thickness, (ii) constant ice/core volume ratio (QCDE), and (iii) stochastic mixing (CSDE).

remaining calculations. This CSDE stochastic mixing aims at simulating the aggregation of many small ice-coated grains. This is formally not the exact situation, as describing the aggregation of thousands of small ice-coated grains with a fixed mantle to core volume would require a dramatically higher number of DDA dipoles. The mixing described by the model is only an approximation to this, and nor is this a classical effective medium theory approach when one phase is diluted in another matrix phase. Given the high ice to core volume ratio adopted, we are definitely not in a regime of domination of one volume component over the other and we are above the percolation threshold, there are very few, if any, embedded isolated dipoles with one-component properties. This model thus represents a fair compromise to simulate the aggregation of many small ice-coated grains. For CSDE, the number of dipoles can be as low as 2000 because of the relaxed condition on the core-mantle shape. This saves calculation time without compromising the required accuracy. The error tolerance is set to better than 10^{-5}, except for the first wavelength points in the UV-visible where it is better than 10^{-2}, again to speed up the calculations. The accuracy in the UV-visible is thus lower, but high enough to serve for the purpose of radiative transfer calculations. Each dataset required about a week (CSDE) to several weeks (QCDE) of calculation time.

3. Models

3.1. Ice mantle to core volume ratio

The volume ratio between ice mantles and the refractory dust grain core (e.g. Dartois 2006) is given by

$$\frac{V(\mathrm{ice})}{V(\mathrm{sil})} = \left(\frac{M_{\mathrm{ice}}}{\rho_{\mathrm{ice}}} N_{\mathrm{H_2O}}\right) \Bigg/ \left(\frac{M_{\mathrm{sil}}}{\rho_{\mathrm{sil}}} \frac{N_{\mathrm{Si}}}{n_{\mathrm{Si}}}\right) \tag{5}$$

$$\text{with } N_{\mathrm{H_2O}} \approx \frac{\tau_{\mathrm{ice}} \Delta\nu_{\mathrm{ice}}}{A_{\mathrm{ice}}} \quad \text{and} \quad N_{\mathrm{Si}} \approx \frac{\tau_{\mathrm{sil}} \Delta\nu_{\mathrm{sil}}}{A_{\mathrm{sil}}},$$

where M_{ice}, ρ_{ice}, M_{sil}, and ρ_{sil} are the molar mass (g mol^{-1}) and density (g cm^{-3}) for water ice and silicates, respectively. $N_{\mathrm{H_2O}}$ and N_{Si} are the water molecules and silicon atoms in the observed silicates column density, respectively. n_{Si} is the number of silicon atoms in a mole of a given silicate. τ_{ice}, $\Delta\nu_{\mathrm{ice}}$, A_{ice}, τ_{sil}, $\Delta\nu_{\mathrm{sil}}$, A_{sil}, are the line centre optical depth, line FWHM (cm^{-1}) and integrated absorption cross section (cm mol^{-1}) of ice and silicates. $M_{\mathrm{sil}}/(\rho_{\mathrm{sil}} n_{\mathrm{Si}})$ is between about 30 and 40 cm^3 mol^{-1} Si^{-1} for magnesium-rich silicates (Reddy et al. 2005) and $M_{\mathrm{H_2O}}/\rho_{\mathrm{H_2O}}$ is about 19.6 cm^3 mol^{-1} for non-porous ice. Using $\Delta\nu_{\mathrm{H_2O}}(3\ \mu\mathrm{m}) \approx 300\ \mathrm{cm^{-1}}$, $A_{\mathrm{H_2O}}(3\ \mu\mathrm{m}) = 2.10^{-16}$ cm mol^{-1} (Öberg et al. 2007; Gerakines et al. 1995; D'Hendecourt & Allamandola 1986; Hagen et al. 1981), and $\Delta\nu_{\mathrm{sil}}(10\ \mu\mathrm{m}) \approx 300\ \mathrm{cm^{-1}}$, $A_{\mathrm{sil}}(10\ \mu\mathrm{m}) \approx 1.6\text{–}2 \times 10^{-16}$ cm mol^{-1}:

$$f_{\mathrm{vol}} = \frac{V(\mathrm{ice})}{V(\mathrm{sil})} \approx (0.4 \sim 0.66)\frac{\tau_{\mathrm{ice}}}{\tau_{\mathrm{sil}}}. \tag{6}$$

The water ice and silicates optical depths are evaluated with respect to A_V towards many lines of sight, or directly as a ratio in some cases. Bowey et al. (2004) and Rieke & Lebofsky (1985) evaluate $A_V/\tau(\mathrm{silicates}) \approx 19.2$ and $A_V/\tau(\mathrm{silicates}) \approx 16.6$, respectively. Murakawa et al. (2000) gives $\tau(\mathrm{H_2O\ ice}) \approx 0.067\ (A_V - A_{V\,\mathrm{threshold}})$, whereas Whittet et al. (1988) gives $\tau(\mathrm{H_2O\ ice}) \approx 0.093\ (A_V - A_{V\,\mathrm{threshold}})$ and $A_V/\tau(\mathrm{silicates}) \approx 12\text{–}25$. Brooke et al. (1999, 1996). Boogert et al. (2011) evaluates $\tau(\mathrm{silicates}) = 0.36 \pm 0.09 + 0.36 \pm 0.06\ \tau(\mathrm{H_2O})$. Combining the various possibilities, we get $\tau_{\mathrm{ice}}/\tau_{\mathrm{sil}} \approx 0.8\text{–}2.5$, and deduce

$$f_{\mathrm{vol}} \approx 1 \pm 0.5.$$

This value establishes a lower limit to the ice-to-refractory mantle volume ratio, as one should include all ices and recall that one integrates the silicate optical depth along lines of sight where some of the grains are uncoated (in particular where the grain temperatures are above mantle sublimation limits, near protostellar objects). We adopt an ice-to-core volume ratio of 1 in the calculations for the main models. In the additional models including additional pure CO in the mantle, we adopt an additional 0.25 volume ratio of CO with respect to the H_2O:CO_2 ice mantle. In the mixed amorphous carbon/silicates core model, we adopt an amorphous carbon to silicates ratio for the core of 2/3, a ratio close to the one adopted in several interstellar dust models (e.g. Hensley & Draine 2021; Jones et al. 2017; Zubko et al. 2004).

3.2. Dust grain growth and size distribution

A simple analytical dust size distribution to describe the diffuse ISM was given early by Mathis et al. (1977), the so-called MRN distribution, with a power law describing the number density of grains as a function of grain radius, with a minimum radius $a_{\mathrm{min}} \sim 0.005\,\mu$m, and an upper bound $a_{\mathrm{max}} \sim 0.25\,\mu$m. The power law follows $\mathrm{d}n(a) \propto a^{\beta}\mathrm{d}a$, with $\beta = -3.5$. In the dense phases of the Galaxy, dust grains will grow in size: moderately by accreting ice mantles in the cold dense molecular regions, or more significantly by aggregation. A large size increase due to grain growth is expected to be primarily due to aggregation rather than gas-phase freeze out, the latter being unable to provide sufficient material to significantly increase the larger grain sizes (see Dartois 2006 for a discussion). This dense phase is the very first step in initiating the subsequent evolution, which will eventually build large planetesimals in protoplanetary disks.

The aggregation, clustering, and assembling of dust particles leading to grain growth is investigated in literature models. The result of the time-dependent evolution of the dust size distribution is shown in, for example, Silsbee et al. (2020), Paruta et al. (2016), Ormel et al. (2009, 2011), and Weingartner & Draine (2001). In these models, at the very first stage of aggregation,

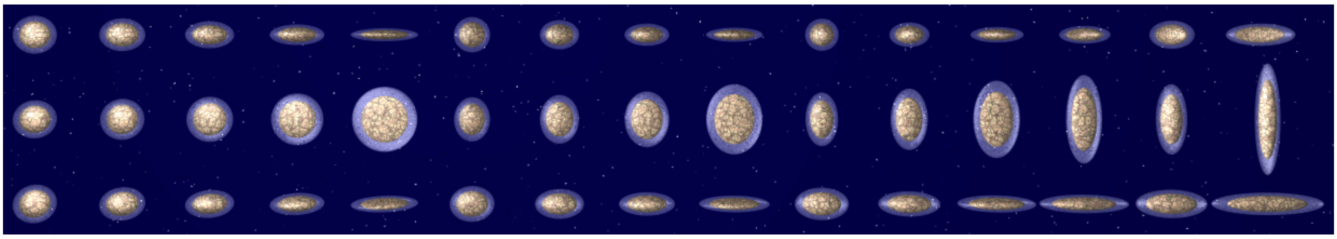

Fig. 3. 3D view of the 15 ellipsoid shapes used in the calculation of the adopted distribution of ice-mantle-coated ellipsoids with a quadratic weighting scheme, as used in Dartois (2006), called CDE2 (e.g. Ossenkopf et al. 1992), presented along their three main axes, as in Fig. 3 of Draine & Hensley (2021). The probability of their occurrence (weighting) in the distribution is the same as in Dartois (2006).

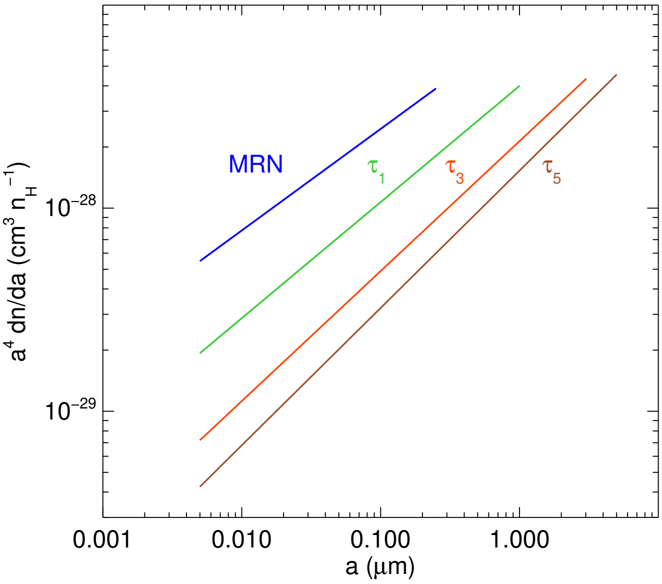

Fig. 4. Size distributions that qualitatively reproduce the expected size evolution behaviour for dust grain growth in aggregation models. The lower bound of the grain sizes is kept constant at 0.005 μm. The upper bound of the distribution is varied from 0.25 μm (MRN distribution) to 1 μm (τ_1), 3 μm (τ_3) and 5 μm (τ_5), and the slope is defined to maintain the same total mass. See text for details.

the size boundaries of the distribution do not move significantly, as there is mostly a redistribution of the most numerous small grains aggregating to other grains of the distribution, and the parameter affected is the slope of the distribution. At larger dynamical times, corresponding to a large fraction of the cloud lifetime, the size distribution shifts towards bigger clustered grains. Starting from the MRN size distribution, we fix a new slope for the power law implying a decrease of the amount of small grains, and calculate the distribution that satisfies two essential criteria: the total mass and the lower size limit in the distribution are conserved. With such calculations, we reproduce qualitatively the range of evolution of the model results presented in, for example, Figs. 2 and 3 of Paruta et al. (2016) or Figs. 4–6 of Silsbee et al. (2020).

Dust grain mass absorption and scattering coefficients are calculated for the three size distributions (MRN, τ_1, τ_3) presented in Fig. 4, for the quadratic ellipsoid weighting scheme (QCDE) and the CSDE, and with an ice mantle to core volume ratio of $f_{\rm vol} = 1$. We apply the model to the M15 (mixture with low CO_2) and M50 (mixture with high CO_2) ice mixtures. We also explore a CSDE model with the M15 ice mixture extended to 5 microns (τ_5), a model with a possible core mixture including amorphous carbon, and a model including a possible pure CO component in the ice mantle. A summary of the models calculated is given in Table 1.

The mass extinction and absorption coefficients are presented in Fig. 5 for different grain sizes for the different sets of models. As expected, the shape of the bands changes when the grain size increases: the bands broaden, become asymmetric and the peak/continuum ratio decreases. The mass coefficients for the different size distribution are presented in Fig. 6. The models show that when grains grow, leading to the τ_1 and τ_3 like size distributions, the anti-symmetric CO_2 ice vibrational mode extinction profile is affected. Averaged over all orientations of the ellipsoids, the mass absorption coefficients behave, to the first order, similarly for the QCDE and CSDE models.

4. Radiative transfer modelling

In order to make relevant comparisons with the expected global mid-infrared spectrum of embedded infrared sources, the UV to millimetre mass extinction coefficient calculated above is used as an input to modelling.

Using the calculated dust distributions, we perform radiative transfer calculations to model the expected spectra from spherical dust clouds and disks, with a higher spectral resolution set on the CO_2 ice profile. The calculations are performed using the Monte Carlo RADMC-3D[1] software (Dullemond et al. 2012), in the full anisotropic scattering mode for the dust radiative transfer.

4.1. Spherical clouds

We model a spherical cloud with an adopted density

$$\rho(r) = \rho_0 (r/r_{\rm in})^{-p},\ r \geq r_{\rm in},\ r \leq r_{\rm out}, \tag{7}$$

where $r_{\rm in}$ is the inner boundary of the cloud and $r_{\rm out}$ the outer one, r is the radial distance to the star, and $\rho(r)$ is the dust density (g cm^{-3}). We also performed DDA calculations for bare silicates to add them into the radiative transfer code for regions where the temperature, determined self-consistently during the radiative transfer calculation, is above the ice sublimation temperature (we adopted $T_{\rm subl} = 100$ K), that is, towards the inner core, and also for the regions where the visual extinction is below a given $A_{\rm V}$ threshold.

We adopted as a model template a prescription close to the one described by Siebenmorgen & Gredel (1997) in the case of HH100 IRS, with $p = 1$, $r_{\rm in} = 0.3$ au, and $r_{\rm out} = 3000$ au. We adjusted the value of ρ_0 to obtain an ice absorption with our conditions close to those observed. Our goal was not to vary all the possible parameters, but to show the effect of the distributions with different levels of grain growth on the CO_2 ice profile.

---

[1] `https://www.ita.uni-heidelberg.de/~dullemond/software/radmc-3d/`

Table 1. Summary of the model parameters in this work.

Set	Model	Ice mantle mixture		Ice mantle mixture				Distribution				Aggregation type	
	#	Silicates	Amorphous carbon	M15	M50	Pure CO	MX	MRN	τ_1	τ_3	τ_5	QCDE	CSDE
A	1	✓		✓				✓				✓	
	2	✓		✓					✓			✓	
	3	✓		✓						✓		✓	
B	4	✓		✓				✓					✓
	5	✓		✓					✓				✓
	6	✓		✓						✓			✓
	7	✓		✓							✓		✓
C	8	✓			✓			✓				✓	
	9	✓			✓				✓			✓	
	10	✓			✓					✓		✓	
D	11	✓			✓			✓					✓
	12	✓			✓				✓				✓
	13	✓			✓					✓			✓
E	14	✓	✓	✓				✓					✓
	14	✓	✓	✓					✓				✓
	16	✓	✓	✓						✓			✓
F	17	✓		✓		✓		✓					✓
	18	✓		✓		✓			✓				✓
	19	✓		✓		✓				✓			✓
G	20	✓					✓	✓					✓
	21	✓					✓		✓				✓
	22	✓					✓			✓			✓

The ice onset threshold is distinct for different clouds and different ices (e.g. Whittet et al. 1988; Murakawa et al. 2000; Boogert et al. 2015, and references therein). The minimum onset value for water ice and quiescent clouds is about 3 (the measured value includes back and front of the cloud and thus correspond to about $A_V^{th} \sim 1.5$ on one side). This threshold value can be higher in other clouds (e.g. Serpens and rho Ophiuchus) with higher thresholds up to above 10 (Tanaka et al. 1990; Eiroa & Hodapp 1989) related to some star formation activity or higher local external UV field. For disks, the typical threshold value is not well known yet, and, if the underlying physics is the same, the equilibrium threshold value might be higher. We thus adopt a visual extinction threshold value $A_V^{th} = 3$ that will be used for both spherical clouds and disk models to keep this parameter fixed for comparison, and in a few models only we explored a threshold of $A_V^{th} = 1.5$. Results of the calculations are shown in Figs. 7–8 for MRN to τ_5 icy dust size distributions with an M15 mantle, τ_3 with an M50 mantle, a model including amorphous carbon in the refractory core, and a model including pure CO in the mantle, for different total column densities corresponding to visual extinctions $A_V^{total} \approx 15, 30, 60, 100$.

4.2. Disks

We model protoplanetary disks at various inclination angles along the line of sight. The axisymmetric disk model parametrisation is given by

$$n(r,z) = n(r)\mathrm{e}^{-(\frac{z}{H(r)})^2},\ r \geq r_{\rm in},\ r \leq r_{\rm out} \tag{8}$$

$$n(r) = n_0(r/r_0)^{-\rm s},\ H(r) = H_0(r/r_0)^{\rm h}, \tag{9}$$

where r is the radial distance to the star and z the height from the disk midplane, $n(r,z)$ the gas density and $H(r)$ is the hydrostatic scale height. We assume a gas-to-dust ratio of 100. We adopt typical values for the parameters of the disk being considered (e.g. Dartois et al. 2003; Piétu et al. 2007; Pinte et al. 2008; Ansdell et al. 2016; Simon et al. 2000): r_0 is set at 100 au, $r_{\rm in} = 0.1$ au, $r_{\rm out} = 100$ au, a value of 1.2 for the hydrostatic scale height exponent, $H_0 = 20$ au, defining the flaring of the disk, and $s = 3$ for the radial density exponent. The density of the disk at 100 au in the mid-plane, n_0, is of the order of 5×10^8 cm^{-3}, corresponding to a total mass for the disk of about 0.02 $M_\odot$. In the radiative transfer code, the region where ices are present is defined with two simultaneous constraints: T must be below the ice sublimation temperature (set to 100 K) and the visual extinction must be above a given A_V threshold (following the fact that thresholds are observed in dark clouds for ice appearance, as mentioned previously). For the region where the visual extinction is below the given A_V threshold or the temperature above ice sublimation, we use bare silicate grains. We use a 3D Cartesian grid with 128^3 points. To provide a better sampling of the inner disk region, the grid is refined first with an inner grid of 32^3 points (a linear factor of 2, factor 8 in volume). This refined inner grid is refined again in the 8^3 points of this sub-grid (linear factor of 2, factor 8 in volume). A sketch of the disk model is shown in Fig. 9.

Results of the calculations as observed for different disk inclinations above the onset of ice absorption, for the different models of the ice and core composition, and dust size distribution are shown in Figs. 10–11. A high diversity of CO_2 ice absorption profiles can be observed for different disk inclinations, column density and extent of grain growth, sometimes showing a marked asymmetry.

5. Discussion

5.1. Optical depth profiles

Observed ice absorption close-ups are often displayed on an optical depth scale, a display that allows for a direct view of the column density involved and the profile of the core of an

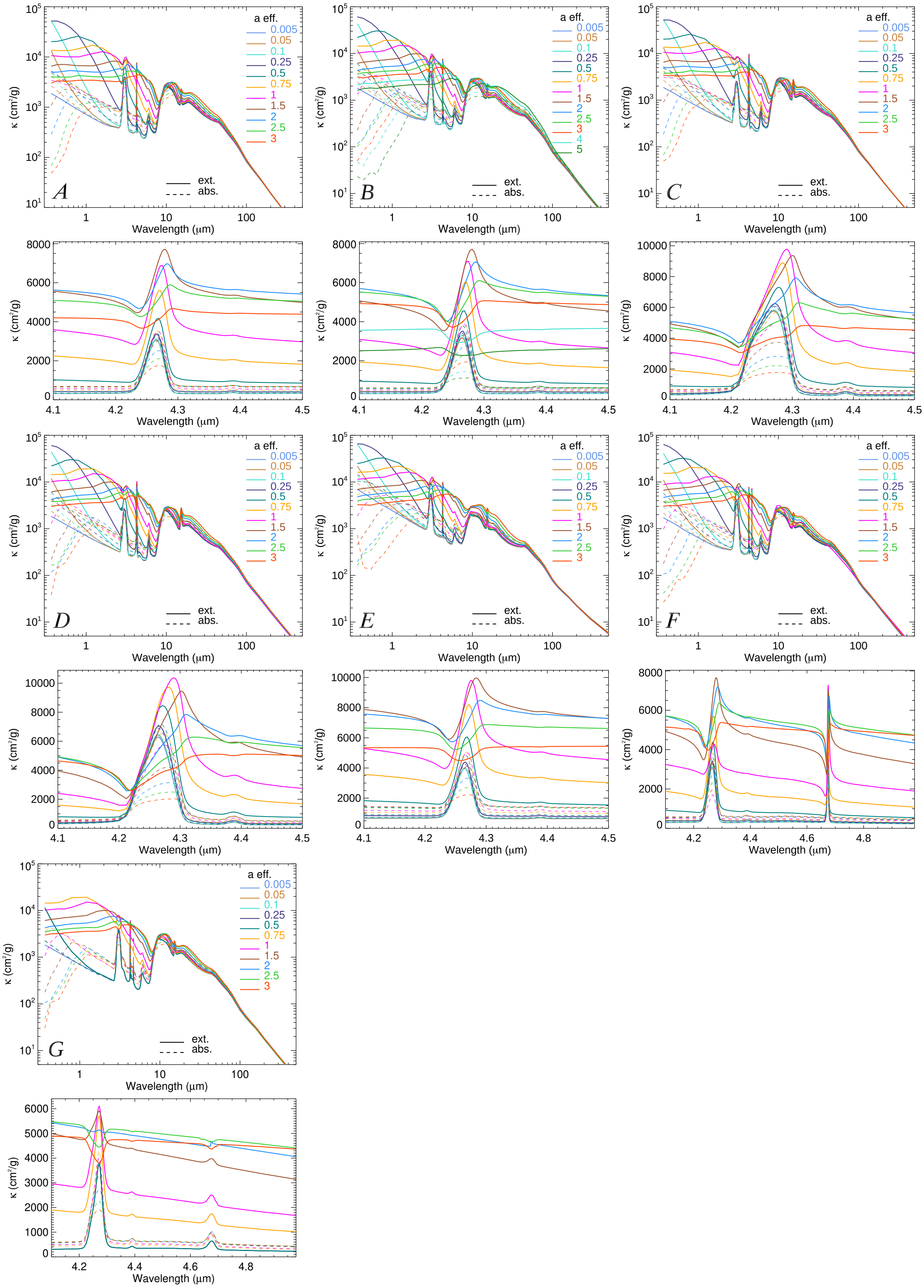

Fig. 5. Grain-size-dependent mass extinction coefficients (solid lines) and absorption coefficients (dashed line) for model compositions corresponding to model sets *A, B, C, D, E, F*, and *G*, from the upper left to the lower right, respectively. The mass extinction coefficients for increasing effective grain radius $a_{\rm eff}$ are shown. See text for details. For each set, a close-up of the CO_2 stretching mode is shown below it (for the last two panels, this also includes CO).

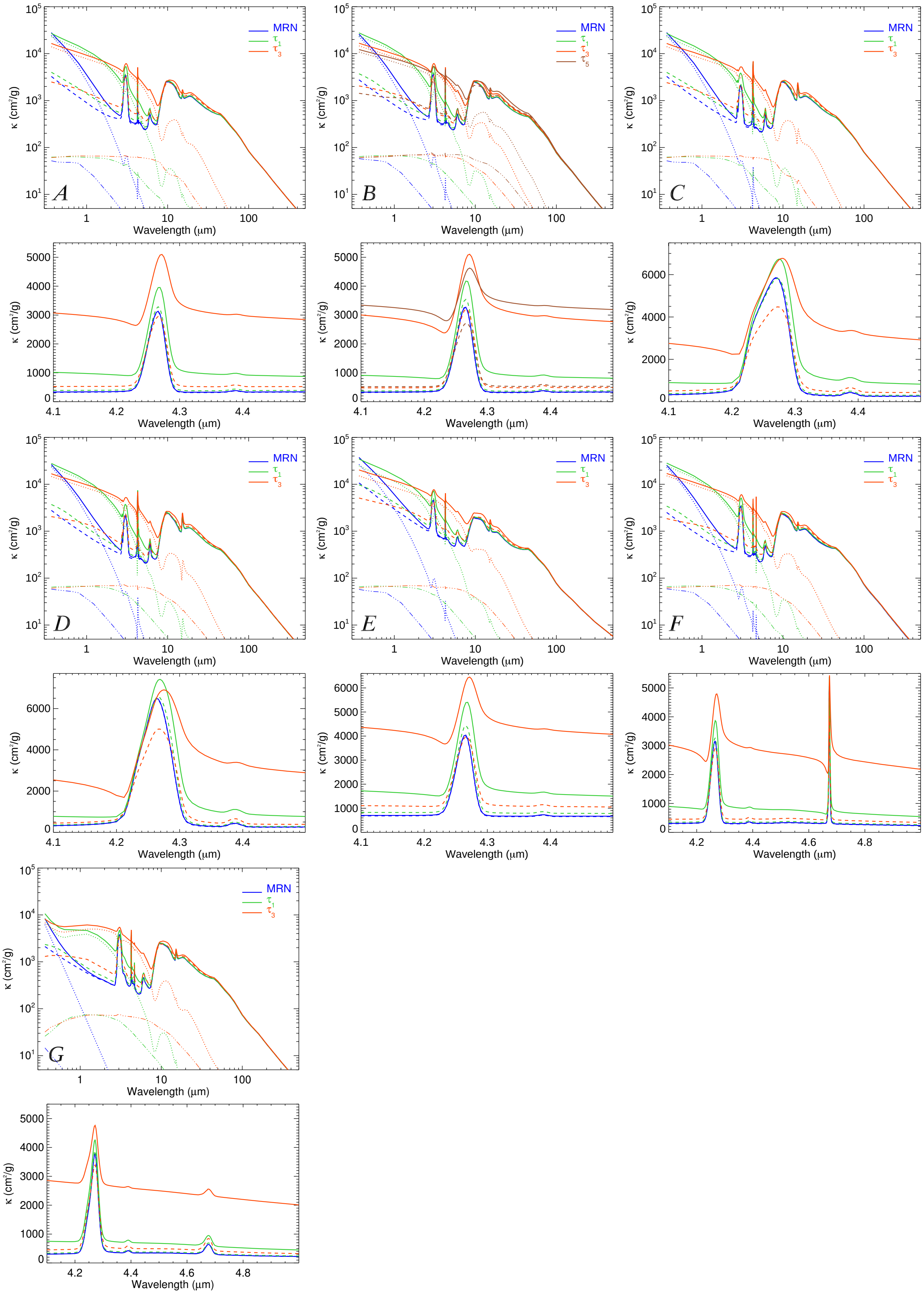

Fig. 6. Mass extinction coefficients (solid lines), absorption coefficients (dashed line), and Henyey–Greenstein phase function g (dot-dashed line, ×100) for model sets *A, B, C, D, E, F*, and *G* (three models per panel corresponding to the MRN ($a_{\max} = 0.25 \mu$m), τ_1 ($a_{\max} = 1 \mu$m), and τ_3 ($a_{\max} = 3 \mu$m) size distributions, respectively). Model set *B* includes a size distribution extending to τ_5 ($a_{\max} = 5 \mu$m). Below each panel a close-up of the CO_2 stretching mode is shown (which includes CO for the last two sets).

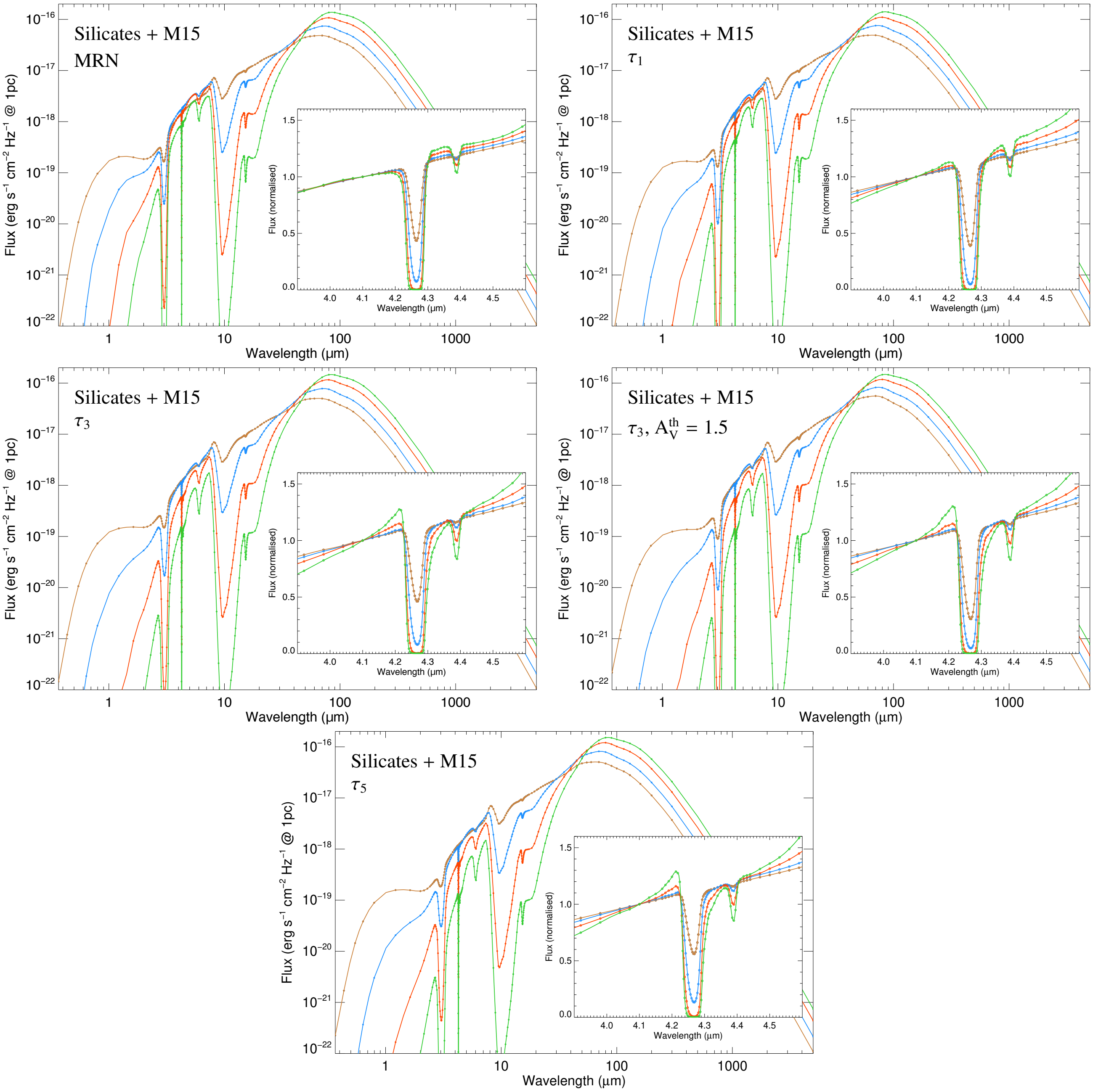

Fig. 7. Spectral energy distributions for the spherical radiative transfer for the M15 ice and core composition, with varying dust size distribution, for different visual extinctions (A_V = 15, brown; 30, blue; 60, red; 100, green). Distributions correspond to, *from the top left to lower right*: silicate core, M15 ice mantle composition and size distribution MRN, and $a_{\max}$ = 0.25 μm (model #4); τ_1, $a_{\max}$ = 1 μm (model #5); τ_3, $a_{\max}$ = 3 μm (model #6); τ_3, $a_{\max}$ = 3 μm (model #6) with ice threshold is set at A_V^{th}(ice) = 1.5 instead of 3; and τ_5, $a_{\max}$ = 5 μm (model #7). The inserts display close-ups of the CO_2 ice band, with spectra normalised at 4.1 μm.

absorption band. However, prior evaluation of a local continuum is required to extract such an optical depth plot. This continuum estimate can seriously modify the original profile, especially in the profile wings. It tends to minimise the structures in these wings, which are expected to be less intense than the core of the absorption. Therefore, it would be desirable, for a better understanding, to display more systematically the observed astronomical features both on a linear flux scale and the extracted optical depth to be able to compare both the core and wings of profiles. It would also be useful to extend the wavelength range of the display to several times that of the core of the absorption in order to understand the continuum flux behaviour.

The use of such a continuum extraction must be made in regards to the aims of the analysis. For column density studies it is a way to extract reasonably good first-order numbers for dense clouds. In the case of the occurrence of intermolecular interactions, the observable effects are often significant enough on the core of the profile that it remains a valid way to proceed, at least as a first step.

We display some examples of observed astronomical infrared spectra of CO_2 ice profiles, recorded mainly towards massive YSO lines of sight, some of them presenting a slightly warped profile. These spectra are displayed in Fig. 12. A linear baseline passing through continuum points on each side

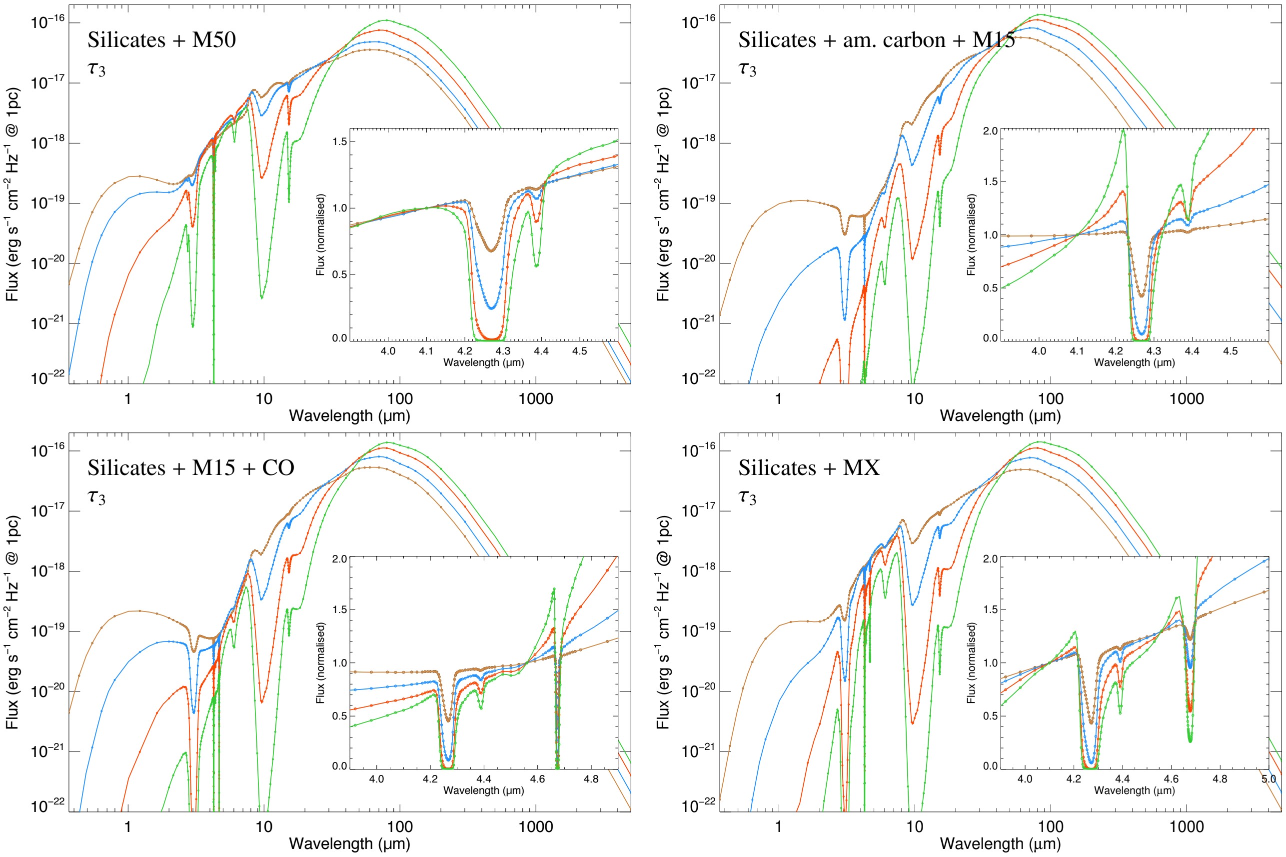

Fig. 8. Same as Fig. 7 but including the other models considered for the ice and core composition. Shown *from the top left to the lower right* are: silicate core, M50 ice mantle composition and size distribution τ_3, $a_{\max} = 3 \mu m$ (model #13); silicates and amorphous carbon core, M15 ice composition, and size distribution τ_3, $a_{\max} = 3$ µm (model #16); silicate core, M15 ice mantle composition, including pure CO and size distribution τ_3, $a_{\max} = 3$ µm (model #19); and silicate core, MX ice mantle composition, including H2O, CO2, CO, and NH3, and size distribution τ_3, $a_{\max} = 3$ µm (model #22). The inserts display close-ups of the CO_2 ice band (and CO for models #19,22), with spectra normalised at 4.1 µm (4.55 µm for models #19,22).

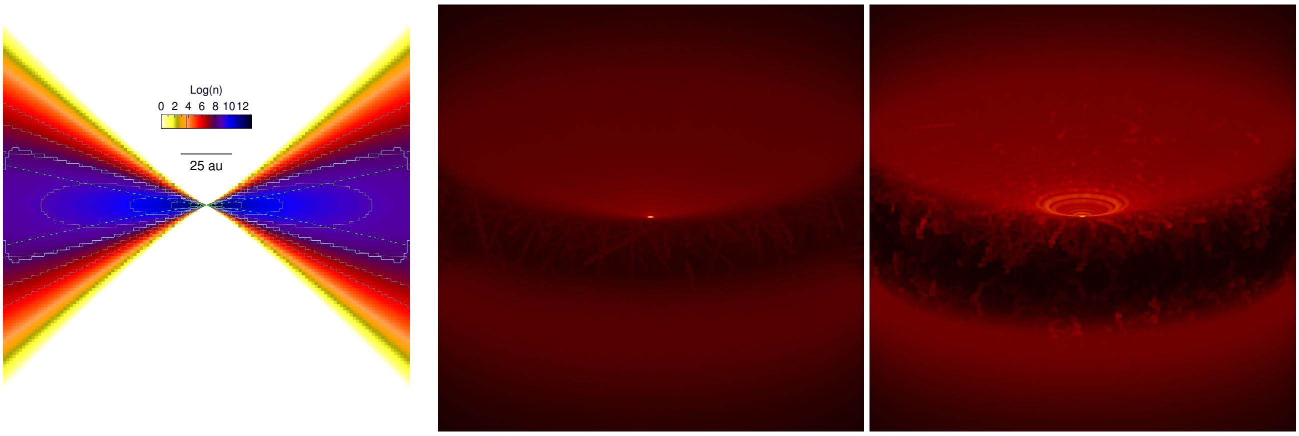

Fig. 9. Disk model and infrared images. *Left panel*: adopted disk model density distribution. The dashed lines show the hydrostatic scale height as a function of distance to the star responsible for the disk flaring. The cyan line defines the boundary of the region where ice mantles are present due to the visual extinction threshold. *Middle and right panels*: RADMC-3D radiative transfer code Monte Carlo images for MRN (*middle*) and τ_3 (*right*) size distributions, ray traced at a wavelength of 4 µm, for the silicates + M15 ice mixture disk model, at an inclination of 72°.

(indicated by circles) far from the band centre, to avoid removing the wings of the absorption profile, is plotted in each panel. This allows us to show the various degrees of band asymmetry.

These CO_2 ice mantle spectra were mainly extracted from the Infrared Space Observatory Short Wavelength Spectrometer (ISO-SWS) spectra database. The criteria to include them here was principally based on the achieved signal-to-noise ratio, in order to minimise spurious statistical effects. They thus comprise moderate resolution SWS06 and SWS01 (scanning speed 3 and 4) astronomical observation templates (AOTs), with a spectral resolution between about 1000 and 3000. We focus here on the CO_2 anti-symmetric stretching mode due to its relatively

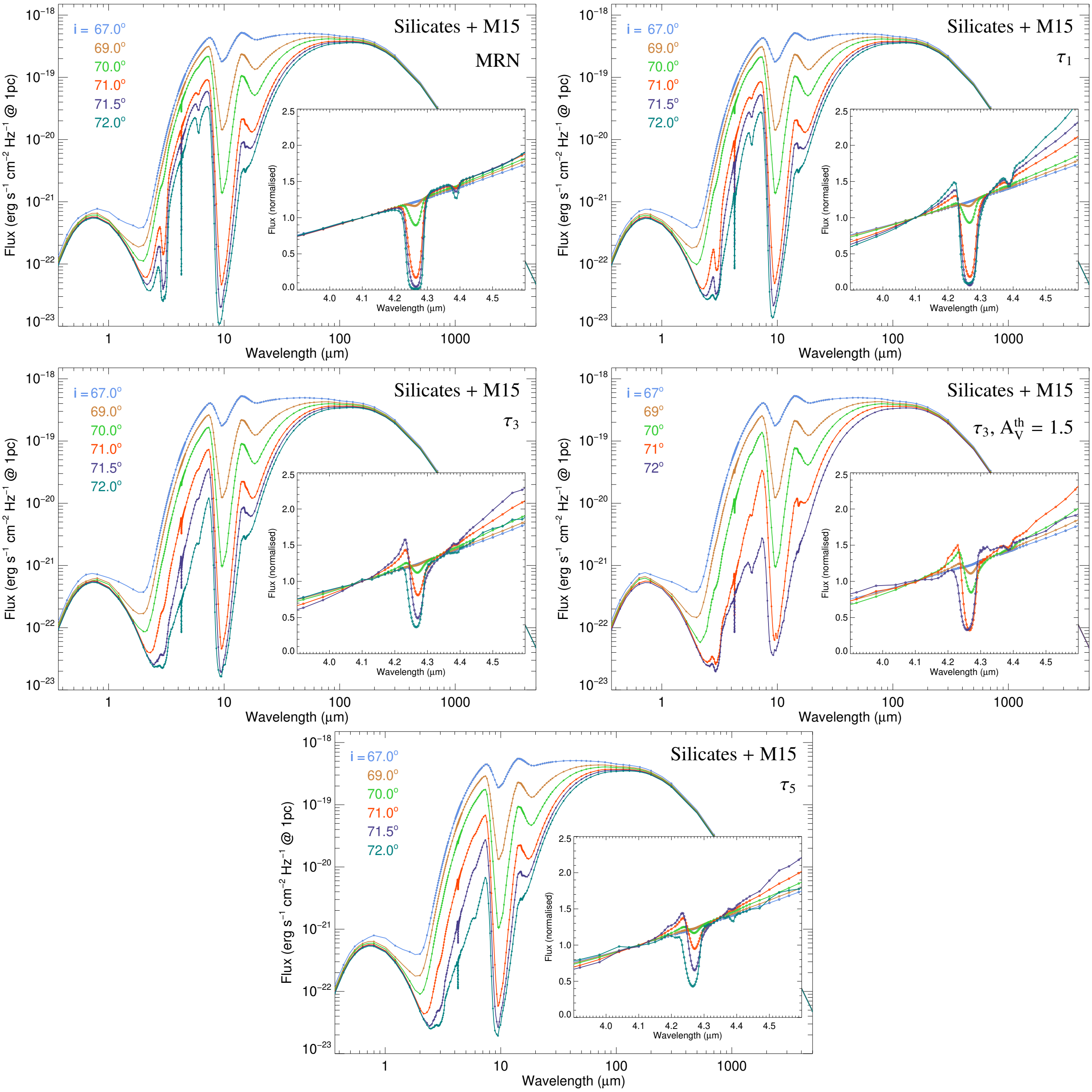

Fig. 10. Spectra of the disk radiative transfer model as observed under different disk inclinations for the M15 ice and core composition and different dust size distributions. Distributions correspond to, *from the top left to the lower right*: silicates core, M15 ice mantle composition and size distribution MRN, $a_{\max}$ = 0.25 µm (model #4); τ_1, $a_{\max}$ = 1 µm (model #5); τ_3, $a_{\max}$ = 3 µm (model #6); τ_3, $a_{\max}$ = 3 µm (model #6) with the ice threshold is set at A_V^{th}(ice) = 1.5 instead of 3; and $a_{\max}$ = 5 µm (model #7).

strong integrated intensity (7.6×10^{-17} cm mol^{-1} Gerakines et al. 1995) over a restricted wavenumber range (~20 cm^{-1}), making it an ideal probe of grain size optical effects. The corresponding source list details are provided in Table A.1.

Upon inspection of Fig.12 it can be seen that in many spectra the blue wing is raised with respect to a linear continuum whereas the red wing is lowered, as if these profiles were the sum of a dominant and symmetric strong absorption profile and a less intense derivative profile. This is such a true profile that is erased when a second-order polynomial continuum fit is forced to lie above every point to avoid giving rise to an 'apparent negative absorption'. In addition, such a forced continuum fit sometimes produces artificial extended wing profiles.

In Fig. 13, we zoom in on spectra of two of the sources presented in Fig. 12, and compare them to spherical radiative transfer results from Fig. 7. In the upper panels, a straight continuum baseline passing through points located at several times the band-FWHM from the band centre (magenta) is over-plotted, as well as spherical cloud radiative transfer model outputs for the M15 mixture, previously presented in Fig. 7, with different distribution upper size limits (MRN,green; τ_1, red; τ_3, blue; τ_5, brown) scaled by an arbitrary common factor for each source observed. The same comparison is presented below in transmittance,

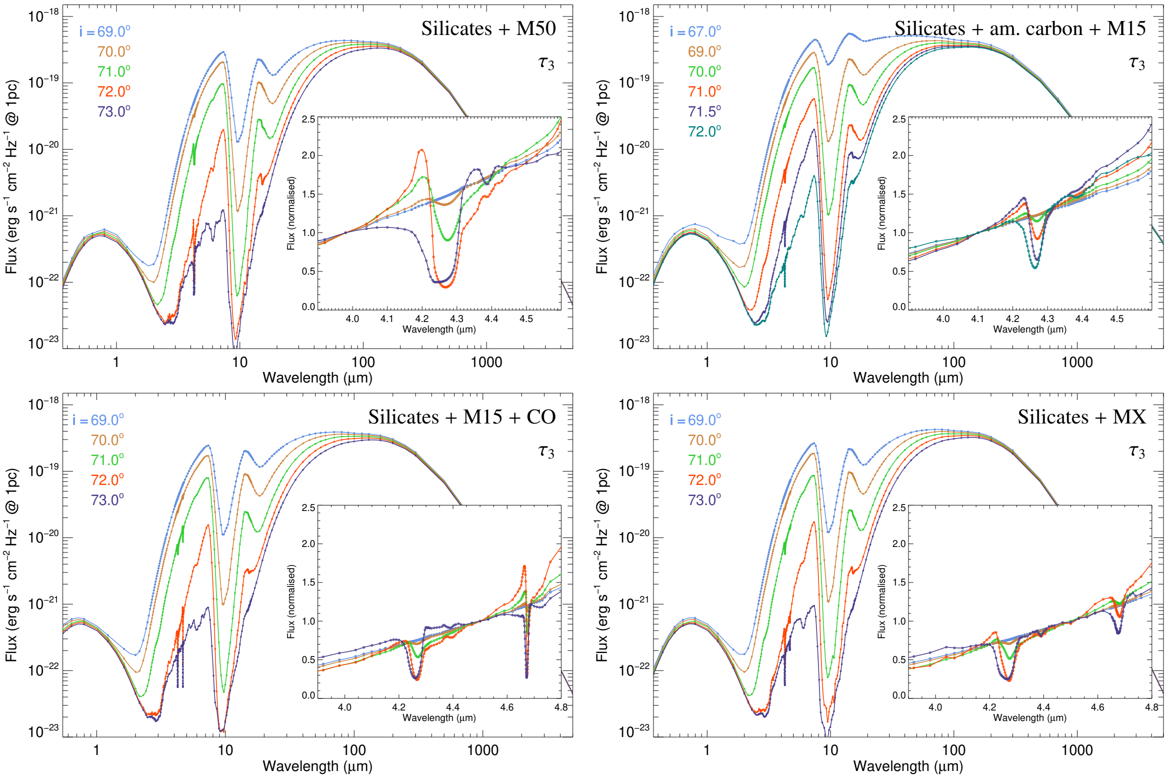

Fig. 11. Spectra of the disk radiative transfer model as observed under different disk inclinations, for different considered models for the ice and core composition, and dust size distribution. Distributions corresponding to, *from top left to lower right*: silicates core, M50 ice mantle composition and size distribution τ_3, $a_{\max}$ = 3 μm (model #13); silicates and amorphous carbon core, M15 ice composition and size distribution τ_3, $a_{\max}$ = 3 μm (model #16); silicates core, M15 ice mantle composition, including pure CO and size distribution τ_3, $a_{\max}$ = 3 μm (model #19); silicates core, MX ice mantle composition and size distribution τ_3, $a_{\max}$ = 3 μm (model #22).

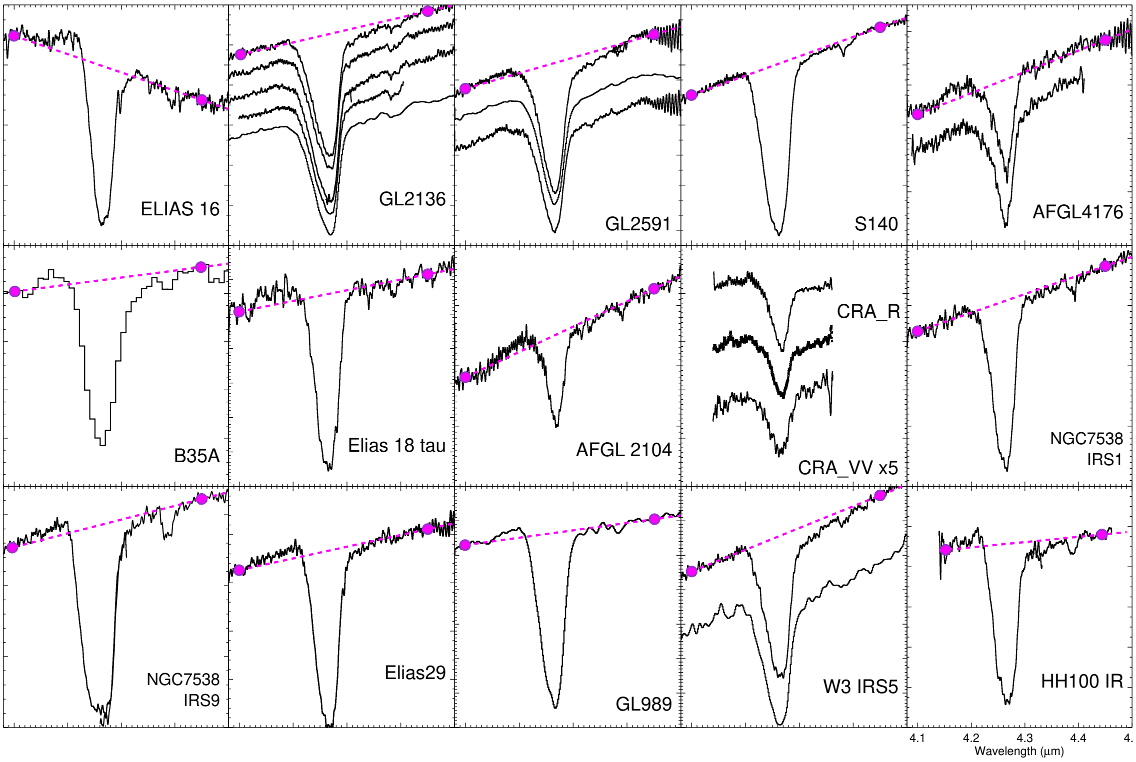

Fig. 12. Diversity of CO_2 anti-symmetric stretching mode observed fluxes with the Infrared Space Observatory (ISO) and Akari (source B35A) towards various astronomical lines of sight, including many massive protostellar objects. The profiles vary with some showing slightly warped asymmetric shapes (e.g. GL2591, B35A, Elias 29, GL989, HH100 IR, and NGC7538). A linear baseline passing through continuum points on each side, far from the band centre, indicated by circles, is plotted in each panel to show the various degrees of band asymmetry.

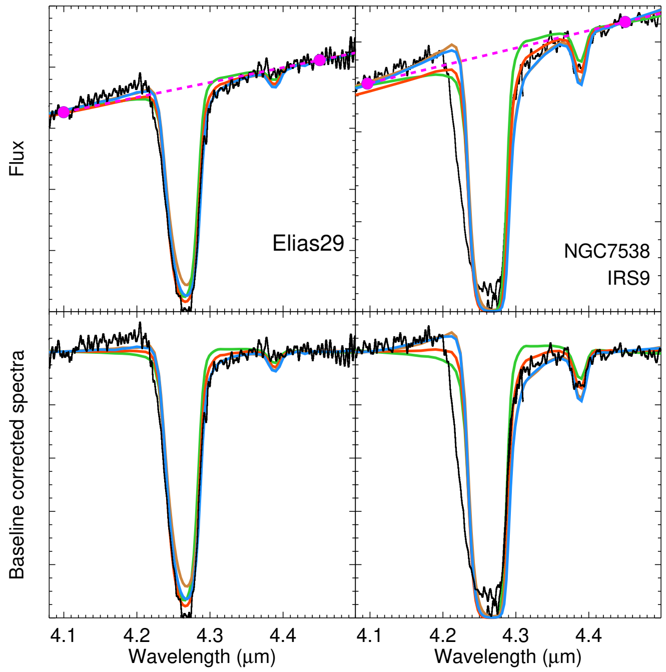

Fig. 13. Example of the comparison of two sources spectra with spherical clouds models. *Upper panels*: CO_2 anti-symmetric stretching mode observed fluxes with the ISO for Elias 29 and NGC7538 IRS9. A straight continuum baseline passing through points located at several times the band-FWHM from the band centre (magenta) is over-plotted, as well as spherical cloud radiative transfer models outputs for M15 mixture presented in Fig. 7 with different distribution upper size limits (MRN (green), τ_1 (red), τ_3 (blue), τ_5 (brown)) scaled by an arbitrary (but common) factor for each observation. For Elias 29, the model spectra are for total visual extinction of 30. For NGC7538 IRS9, the model spectra are for total visual extinction of 60. *Lower panels*: same comparison but in transmittance, after baseline correction applied to each spectrum, which minimises baseline effects in the comparison.

after linear baseline corrections applied to each model and the observational spectrum, which minimises baseline effects in the comparison. It is not a fit performing an inversion model for each of these sources, which is beyond of the scope of this article, but rather is designed to allow us to compare the evolution of the profiles. It should be noted that for the distribution with an upper bound at 5 microns in size, when compared to that at 3 microns, the profile evolution is less pronounced. Indeed, the grains getting bigger contribute as an almost flat extinction in a spherical cloud model (i.e. their cross section approaches their geometrical cross section), as can be deduced from the individual grain mass absorption contributions presented in Fig. 5, model B. This can be observed in the comparison with the Elias 29 source for which the core of the CO_2 band in the τ_5 model absorbs comparatively less. The observed profiles are compatible with a size increase of the size upper bound in the 1–3 µm range (with the adopted size distributions presented in Fig. 4). The early stages of coagulation and eventual further growth is suggested by other observables such as the near infrared scattering properties and coreshine or cloudshine effects (e.g. Saajasto et al. 2021; Ysard et al. 2016, and references therein).

In the case of the few observed edge-on disks (e.g. Terada & Tokunaga 2017), with profiles departing from classical ice band profiles observed in the progenitor phases such as dense clouds, partly due to eventual composition and phase change where it is probed, and partly due to grain growth, this baseline correction will affect the interpretation. The global effect of grain growth on the CO_2 ice stretching mode profile is an observable distortion with a rise in the blue wing around 4.2 µm and an absorbing red wing. Such a slight warping of the profiles is already observed in clouds and envelopes surrounding YSOs and confirms the presence of grain sizes larger than those found in the diffuse ISM in the grain size distribution, following grain coagulation.

In Fig. 14, we display close-ups of the CO_2 spectra of the disk radiative transfer model with M15 ice mantle composition and MRN size distribution, with $a_{\rm max}$ = 0.25 µm (model #4); τ_1, $a_{\rm max}$ = 1 µm (model #5); τ_3, $a_{\rm max}$ = 3 µm (model #6); τ_5, $a_{\rm max}$ = 5μm (model #7); as observed at different disk inclinations. The spectra are again analysed with a linear baseline drawn from 4.1 to 4.45 µm on the flux spectra (shown normalised at 4.1 µm because of large flux differences at the various inclinations). From the baseline corrected spectra, the evolution of the optical depth in the ice absorption core (4.27 µm), in the blue wing (4.22 µm), and in the red wing (4.31 µm) are given as a function of inclination to evaluate the degree of warping of the band.

The way local continuum baselines have generally been applied to extract the absorption profile may erase this subtle information that is sometimes only present in the wings of the profile. The profile resulting from such a baseline correction is then analysed with the sum of different ice mixture contributions using a principal component spectral deconvolution, whereas the reality is rather a more complex combination of grain size and composition effects affecting the profile when grains grow significantly in the distribution.

In the case of protoplanetary disks, as shown in our calculations, the emerging ice profiles will appear even more affected than for spherical envelopes or dense clouds. Profiles that seem even reversed, with a pronounced blue-shifted wing absorption, in disks, for high inclination and thus high optical depth, have been observed (e.g. IRAS04302+2247, Aikawa et al. 2012, Fig. 3), as observed in some models of Figs. 10–11.

5.2. CO_2 and CO profiles

CO and CO_2 stretching modes both fall within a relatively narrow wavelength range. In the case of CO and CO_2 mixed in the same ice mantles or on the same grains in the dust size distribution, if the grain growth dominates over the influence of the intrinsic ice mixture composition, both CO_2 and CO profiles should display a relative common asymmetry in their respective profiles, as seems to be the case in, for example, Noble et al. (2013; Fig. 2d). In the case of pure CO the profile asymmetry might even be more pronounced because of the narrower feature for the large grains in the distribution (see e.g. Dartois 2006).

5.3. H_2O versus CO_2 band profile

The spectra extracted from the disk models with an M15 ice mantle composition and the different size distributions are shown in Fig. 15, spanning the water ice and carbon dioxide stretching modes range. The profile distortion observed in the CO_2 stretching mode is also observed in the water ice band, with a red shift of its band centre as well as the occurrence of a red extinction wing. The contrast is less pronounced than for the CO_2 ice band because of the much larger intrinsic band width for this band. Infrared observations in the H_2O, CO_2, and CO stretching mode region for some sources with available coverage and for which the gas-phase CO does not hamper the observation of the CO ice profile are shown in Fig. 16. The profiles of the CO_2 and

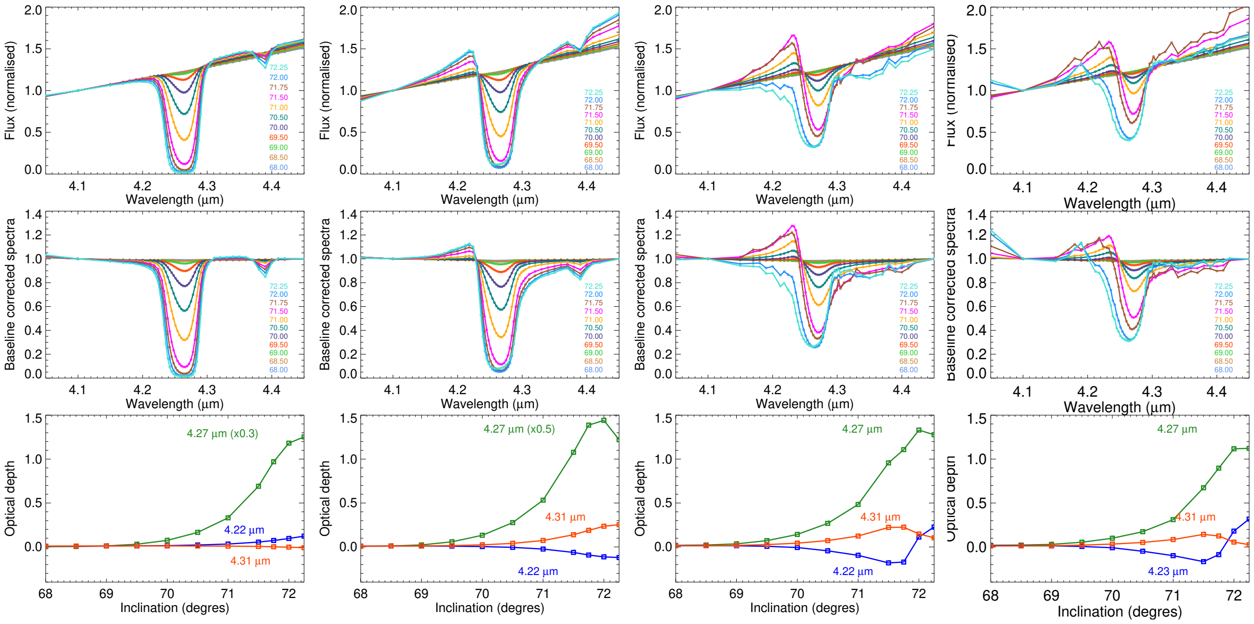

Fig. 14. Zoomed-in view of CO$_2$ spectra of the disk radiative transfer model with M15 ice mantle composition and MRN size distribution, $a_{\rm max}$ = 0.25 μm (model #4); τ_1, $a_{\rm max}$ = 1 μm (model #5); τ_3, $a_{\rm max}$ = 3 μm (model #6); τ_5, $a_{\rm max}$ = 5 μm (model #7); as observed at different disk inclinations. *Top panels*: flux spectra normalised at 4.1 μm. *Middle panels*: linear baseline corrected spectra with baseline reference points taken at 4.1 and 4.45 μm. *Lower panels*: evolution of the optical depth in the core (4.27 μm), the blue wing (4.22 μm), and red wing (4.31 μm) with disk inclination.

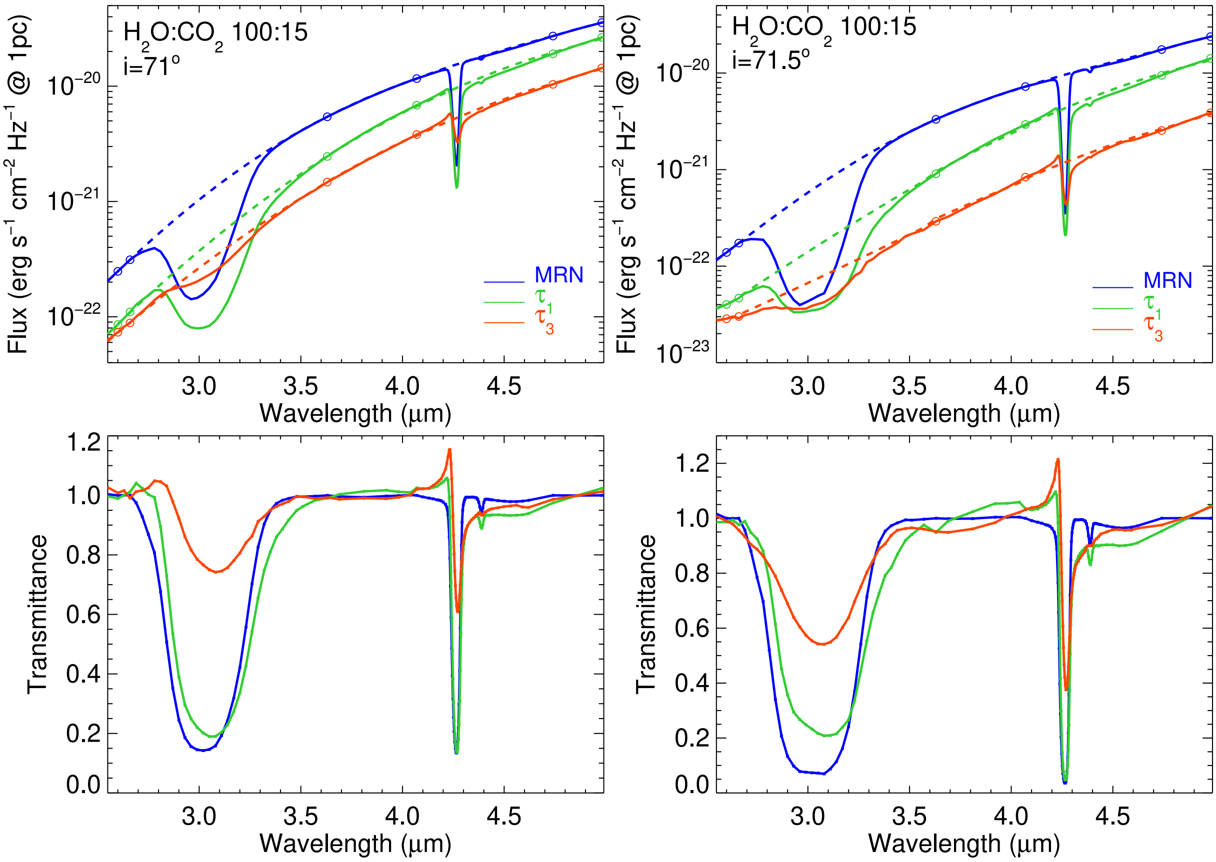

Fig. 15. Close-up of the disk radiative transfer models (*upper panels*) corresponding to silicates core, M15 ice mantle composition and size distribution MRN, $a_{\rm max}$ = 0.25 μm (model #4); τ_1, $a_{\rm max}$ = 1 μm (model #5); τ_3, $a_{\rm max}$ = 3 μm (model #6); as observed under 71 and 71.5 degrees of inclination, in the water ice and carbon dioxide stretching modes range. A spline continuum passing through the indicated circle points, well apart from the core of the ice bands, is overlaid (dashed line). *Lower panels* show the extracted resulting transmittance spectra after dividing by this estimated continuum. In the highest optical depth spectrum (i = 71.5°, τ_3) both the calculated spectrum and a slightly numerical noise filtered spectrum are shown. The asymmetry of the water ice band as well as the shift in the band centre are evidenced and accompanies the observed higher contrast CO$_2$ profile deformation.

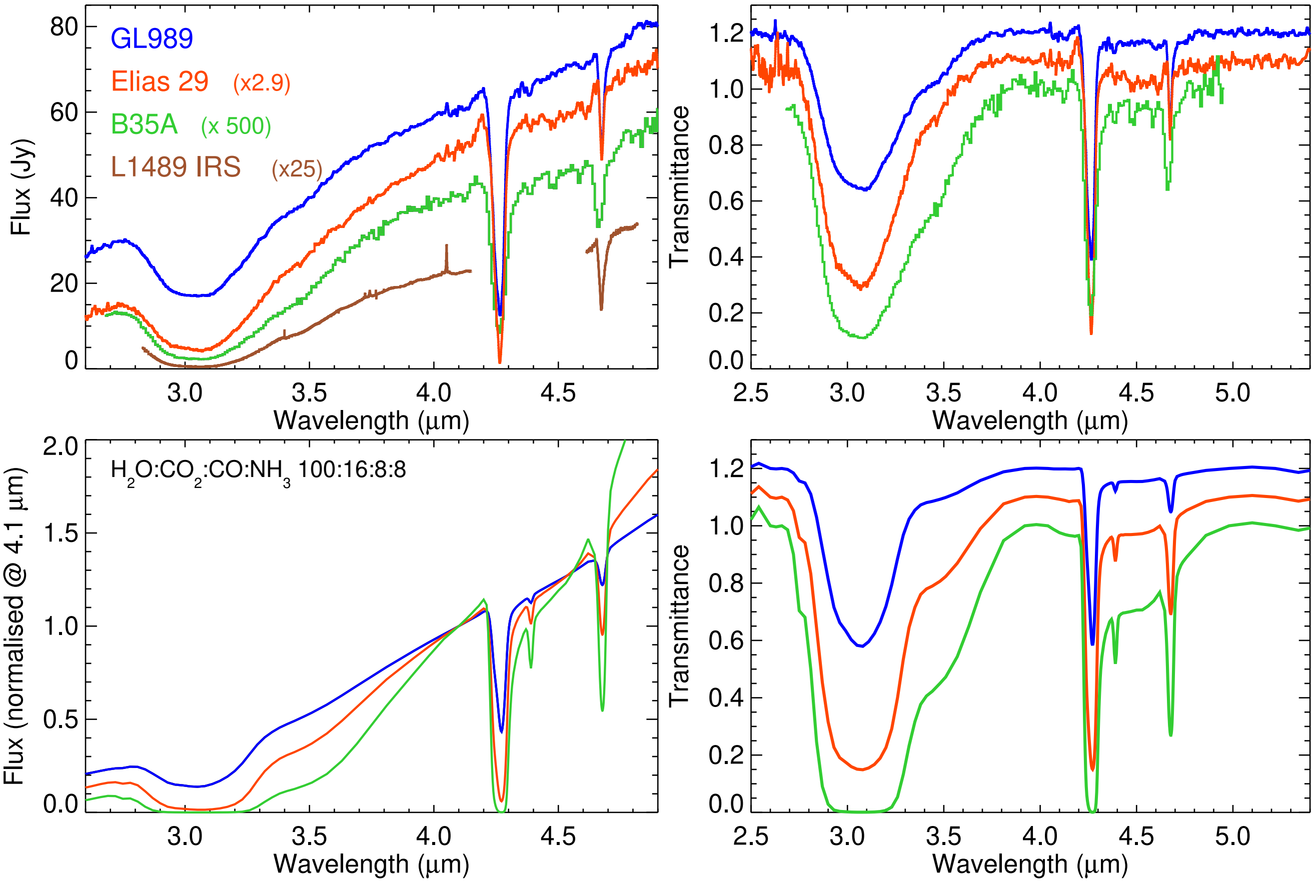

Fig. 16. Comparison between YSOs observations and models. *Upper left*: infrared observations in the H_2O, CO_2, CO stretching mode region for some sources with available coverage and for which gas-phase CO does not hamper observation of the CO ice profile. GL989 and Elias 29 are from the ISO database, B35A is an Akari spectrum (Noble et al. 2013), L1489 IRS is ground-based high resolution spectra from Boogert et al. (2002). In the L1489 spectrum, the gas-phase CO has been filtered out to show the CO ice profile. *Lower left*: spherical cloud model spectra with the MX mixture for a τ_3 size distribution, for cloud visual extinction of Av = 15 (blue), 30 (red), and 60 (green). The *right panels* shown the same observations and models after baseline correction to provide transmittance spectra. The blue and red traces have been offset by 0.2 and 0.1, respectively, for clarity.

CO seem to display an increase at the lower wavelength side of each band, and for H_2O, CO_2 and CO an extinction wing contribution on the higher wavelength side of each band. This stresses the importance of recording ice profiles with a span covering not only the core, but also the surrounding continuum, over several times the band FWHM, in order to accurately constrain the grain growth contribution.

We show for comparison in Fig. 16 spherical cloud model spectra with the more complex ice mixture MX (H_2O:CO_2:CO:NH_3 100:16:8:8) for a τ_3 size distribution, for cloud visual extinction of Av = 15 (blue), 30 (red) and 60 (green). We also display both observations and models after baseline correction to provide transmittance spectra for comparison. The influence of grain growth on the water ice stretching mode profile is necessary to account for the red wing observed in this band towards many lines of sight, as was explored in (e.g. Smith et al. 1988, 1989; Dartois et al. 2002), with the additional contribution from the ammonia hydrate related band around 3.47 µm (also present in the MX ice mixture models), and possibly a smaller contribution from methanol stretching mode at 3.54 µm that is not in the calculations. The MX model spectra reproduces most of the observed features including the red shift of the water ice band centre, the extended red wing in the absorption of CO_2 and CO absorption bands.

6. Conclusion

We have modelled the mass absorption coefficient for interstellar dust grains, including ice mantles, from the classical MRN diffuse ISM dust size distribution to dust populations growing in the denser ISM phases, with increasing amounts of larger grains of up to five microns in size. These models were injected into Monte Carlo radiative transfer calculations for a spherical dense cloud and a protoplanetary axisymmetric disk model. The influence of grain growth on the ice spectroscopic profiles is demonstrated, with a particular focus on the CO_2 ice stretching mode extinction.

Several ice mantle and refractory dust core association possibilities, such as a constant ice/core volume ratio, constant ice thickness, and randomly mixed ice and refractory core aggregations, were modelled. While differences exist among the details of the profiles, the two dominant parameters affecting the results are the influence of large grains in the distributions on the resulting profiles and the chosen starting ice mixture's optical constants, which reflect inter-molecular interactions in the solid phase.

If this grain growth turns out to be significant in the observed disk regions, this study shows it will strongly impact the observed band profiles, and the retrieval of the underlying ice mantle compositions will be more complex than the usually assumed principal component analysis that uses a basis set of planar thin film ice mixture spectra and performed on dense clouds observations.

Sources where grain growth has significantly impacted the dust size distribution should display a set of ice bands with noticeable spectral distortion, particularly in the wings of the bands. Too highly constrained continuum extraction baselines and the resulting spectra shown in optical depth tend to minimise the significance of these distortions. We strongly recommend taking care during baseline subtraction to both use a large spectral window span around the band and to not correct for apparent negative absorption.

Detailed ice profile analyses observed in protoplanetary disks with next-generation observatories, such as the JWST, in particular for the CO$_2$ ice mantle profile, will provide, in comparison to such models, a strong constraint on the extent of grain growth, in the micron range, for the dust distributions.

Acknowledgements. We gratefully acknowledge H. Fraser for kindly providing us the B35A Akari spectrum data. Part of this work was supported by the Programme National “Physique et Chimie du Milieu Interstellaire” (PCMI) of CNRS/INSU with INC/INP co-funded by CEA and CNES.

References

Aikawa, Y., Kamuro, D., Sakon, I., et al. 2012, A&A, 538, A57
Ansdell, M., Williams, J. P., van der Marel, N., et al. 2016, ApJ, 828, 46
Ballering, N. P., Cleeves, L. I., & Anderson, D. E. 2021, ApJ, 920, 115
Boogert, A. C. A., Hogerheijde, M. R., & Blake, G. A. 2002, ApJ, 568, 761
Boogert, A. C. A., Pontoppidan, K. M., Knez, C., et al. 2008, ApJ, 678, 985
Boogert, A. C. A., Huard, T. L., Cook, A. M., et al. 2011, ApJ, 729, 92
Boogert, A. C. A., Gerakines, P. A., & Whittet, D. C. B. 2015, ARA&A, 53, 541
Bowey, J. E., Rawlings, M. G., & Adamson, A. J. 2004, MNRAS, 348, L13
Brooke, T. Y., Sellgren, K., & Smith, R. G. 1996, ApJ, 459, 209
Brooke, T. Y., Sellgren, K., & Geballe, T. R. 1999, ApJ, 517, 883
Chiar, J. E., Ennico, K., Pendleton, Y. J., et al. 2007, ApJ, 666, L73
Dartois, E. 2005, Space Sci. Rev., 119, 293
Dartois, E. 2006, A&A, 445, 959
Dartois, E., Demyk, K., d’Hendecourt, L., & Ehrenfreund, P. 1999a, A&A, 351, 1066
Dartois, E., Schutte, W., Geballe, T. R., et al. 1999b, A&A, 342, L32
Dartois, E., d’Hendecourt, L., Thi, W., Pontoppidan, K. M., & van Dishoeck, E. F. 2002, A&A, 394, 1057
Dartois, E., D’Hendecourt, L., Thi, W. F., Pontoppidan, K. M., & van Dishoeck, E. F. 2003, in Astrophysics of Dust, ed. A. N. Witt, 155
D’Hendecourt, L. B., & Allamandola, L. J. 1986, A&AS, 64, 453
Draine, B. T., & Flatau, P. J. 2000, DDSCAT: The discrete dipole approximation for scattering and absorption of light by irregular particles
Draine, B. T., & Flatau, P. J. 2008, J. Opt. Soc. Am. A, 25, 2693
Draine, B. T., & Flatau, P. J. 2013, ArXiv e-prints, [arXiv:`1305.6497`]
Draine, B. T., & Hensley, B. S. 2021, ApJ, 910, 47
Draine, B. T., & Lee, H. M. 1984, ApJ, 285, 89
Dullemond, C. P., Juhasz, A., Pohl, A., et al. 2012, RADMC-3D: A multi-purpose radiative transfer tool, Astrophysics Source Code Library, [`record ascl:1202.015`]
Ehrenfreund, P., Boogert, A. C. A., Gerakines, P. A., et al. 1996, A&A, 315, L341
Ehrenfreund, P., Boogert, A. C. A., Gerakines, P. A., Tielens, A. G. G. M., & van Dishoeck, E. F. 1997, A&A, 328, 649
Ehrenfreund, P., Kerkhof, O., Schutte, W. A., et al. 1999, A&A, 350, 240
Eiroa, C., & Hodapp, K. W. 1989, A&A, 210, 345
Fabian, D., Henning, T., Jäger, C., et al. 2001, A&A, 378, 228
Gerakines, P. A., Schutte, W. A., Greenberg, J. M., & van Dishoeck, E. F. 1995, A&A, 296, 810
Gibb, E. L., Whittet, D. C. B., Boogert, A. C. A., & Tielens, A. G. G. M. 2004, ApJS, 151, 35
Hagen, W., Tielens, A. G. G. M., & Greenberg, J. M. 1981, Chem. Phys., 56, 367
Hensley, B. S., & Draine, B. T. 2021, ApJ, 906, 73
Honda, M., Inoue, A. K., Fukagawa, M., et al. 2009, ApJ, 690, L110
Hudgins, D. M., Sandford, S. A., Allamandola, L. J., & Tielens, A. G. G. M. 1993, ApJS, 86, 713
Hudson, R. L., Gerakines, P. A., & Moore, M. H. 2014, Icarus, 243, 148
Hudson, R. L., Gerakines, P. A., Yarnall, Y. Y., & Coones, R. T. 2021, Icarus, 354, 114033
Jones, A. P., Köhler, M., Ysard, N., et al. 2016, A&A, 588, A43
Jones, A. P., Köhler, M., Ysard, N., Bocchio, M., & Verstraete, L. 2017, A&A, 602, A46
Keane, J. V., Tielens, A. G. G. M., Boogert, A. C. A., Schutte, W. A., & Whittet, D. C. B. 2001, A&A, 376, 254
Lefèvre, C., Pagani, L., Juvela, M., et al. 2014, A&A, 572, A20
Madden, M. C. L., Boogert, A. C. A., Chiar, J. E., et al. 2022, ApJ, 930, 2
Mathis, J. S., Rumpl, W., & Nordsieck, K. H. 1977, ApJ, 217, 425
Meeus, G. 2011, Earth Moon and Planets, 108, 45
Min, M., Hovenier, J. W., & de Koter, A. 2003, A&A, 404, 35
Moore, M. H., & Hudson, R. L. 1998, Icarus, 135, 518
Murakawa, K., Tamura, M., & Nagata, T. 2000, ApJS, 128, 603
Noble, J. A., Fraser, H. J., Aikawa, Y., Pontoppidan, K. M., & Sakon, I. 2013, ApJ, 775, 85
Öberg, K. I., Fraser, H. J., Boogert, A. C. A., et al. 2007, A&A, 462, 1187
Öberg, K. I., Boogert, A. C. A., Pontoppidan, K. M., et al. 2011, ApJ, 740, 109
Ormel, C. W., Paszun, D., Dominik, C., & Tielens, A. G. G. M. 2009, A&A, 502, 845
Ormel, C. W., Min, M., Tielens, A. G. G. M., Dominik, C., & Paszun, D. 2011, A&A, 532, A43
Ossenkopf, V., Henning, T., & Mathis, J. S. 1992, A&A, 261, 567
Palumbo, M. E., Baratta, G. A., Collings, M. P., & McCoustra, M. R. S. 2006, Phys. Chem. Chem. Phys. (Incorporating Faraday Trans.), 8, 279
Palumbo, M. E., Baratta, G. A., Fedoseev, G., et al. 2020, in Laboratory Astrophysics: From Observations to Interpretation, 350, eds. F. Salama, & H. Linnartz, 350, 77
Paruta, P., Hendrix, T., & Keppens, R. 2016, Astron. Comput., 16, 155
Piétu, V., Dutrey, A., & Guilloteau, S. 2007, A&A, 467, 163
Pinte, C., Ménard, F., Berger, J. P., Benisty, M., & Malbet, F. 2008, ApJ, 673, L63
Pontoppidan, K. M. 2006, A&A, 453, L47
Pontoppidan, K. M., Dullemond, C. P., van Dishoeck, E. F., et al. 2005, ApJ, 622, 463
Rachid, M. G., Terwisscha van Scheltinga, J., Koletzki, D., & Linnartz, H. 2020, A&A, 639, A4
Reddy, R., Gopal, K. R., Ahammed, Y. N., et al. 2005, Solid state Ionics, 176, 401
Rieke, G. H., & Lebofsky, M. J. 1985, ApJ, 288, 618
Rouleau, F., & Martin, P. G. 1991, ApJ, 377, 526
Saajasto, M., Juvela, M., & Malinen, J. 2018, A&A, 614, A95
Saajasto, M., Juvela, M., Lefèvre, C., Pagani, L., & Ysard, N. 2021, A&A, 647, A109
Satorre, M. Á., Domingo, M., Millán, C., et al. 2008, Planet. Space Sci., 56, 1748
Siebenmorgen, R., & Gredel, R. 1997, ApJ, 485, 203
Silsbee, K., Ivlev, A. V., Sipilä, O., Caselli, P., & Zhao, B. 2020, A&A, 641, A39
Simon, M., Dutrey, A., & Guilloteau, S. 2000, ApJ, 545, 1034
Smith, R. G., Sellgren, K., & Tokunaga, A. T. 1988, ApJ, 334, 209
Smith, R. G., Sellgren, K., & Tokunaga, A. T. 1989, ApJ, 344, 413
Steinacker, J., Andersen, M., Thi, W. F., et al. 2015, A&A, 582, A70
Tanaka, M., Sato, S., Nagata, T., & Yamamoto, T. 1990, ApJ, 352, 724
Tazaki, R., Murakawa, K., Muto, T., Honda, M., & Inoue, A. K. 2021a, ApJ, 910, 26
Tazaki, R., Murakawa, K., Muto, T., Honda, M., & Inoue, A. K. 2021b, ApJ, 921, 173
Terada, H., & Tokunaga, A. T. 2017, ApJ, 834, 115
Terada, H., Tokunaga, A. T., Kobayashi, N., et al. 2007, ApJ, 667, 303
Terwisscha van Scheltinga, J., Ligterink, N. F. W., Boogert, A. C. A., van Dishoeck, E. F., & Linnartz, H. 2018, A&A, 611, A35
Trotta, F. 1996, PhD thesis Université Joseph Fourier, Grenoble, France
van Boekel, R., Min, M., Waters, L. B. F. M., et al. 2005, A&A, 437, 189
van Breemen, J. M., Min, M., Chiar, J. E., et al. 2011, A&A, 526, A152
van Dishoeck, E. F. 2004, ARA&A, 42, 119
Warren, S. G. 1984, Appl. Opt., 23, 1206
Weingartner, J. C., & Draine, B. T. 2001, ApJ, 548, 296
Whittet, D. C. B., Bode, M. F., Longmore, A. J., et al. 1988, MNRAS, 233, 321
Ysard, N., Köhler, M., Jones, A., et al. 2016, A&A, 588, A44
Ysard, N., Jones, A. P., Demyk, K., Boutéraon, T., & Koehler, M. 2018, A&A, 617, A124
Zubko, V., Dwek, E., & Arendt, R. G. 2004, ApJS, 152, 211

Appendix A: Observations log

Table A.1. Infrared Space Observatory observations: sources, observation number (TDT), observing template (AOT), and integration time.

Source	TDT #	AOT	Int. time (s)
AFGL 2136	12000925	SWS06	2994
	12800302	SWS06	3732
	31101023	SWS06	4391
	33000222	SWS01	3554
	51601403	SWS06	1404
AFGL 2591	14200503	SWS06	2908
	02800582	SWS06	1972
	35700734	SWS01	3454
	35701221	SWS07	7002
W3 IRS5	42701224	SWS06	5668
	42701302	SWS01	3454
HH100 IR	70400725	SWS06	2616
AFGL 989	71602619	SWS01	3454
AFGL 2104	14900501	SWS06	880
AFGL 4176	11701404	SWS06	1706
	30601344	SWS06	4268
CRA R	12400103	SWS06	862
	71502103	SWS06	862
CRA W	12400406	SWS06	1190
Elias 16	68600538	SWS06	8682
Elias 29	29200615	SWS06	5668
NGC7538 IRS1	28301235	SWS06	4552
NGC7538 IRS9	56801802	SWS06	3328
Elias 18 Tau	68502539	SWS06	3140
S140	26301731	SWS06	5270
GCS 3I	32701543	SWS06	3226

SWS01 and SWS06 spectral resolution are dependent on the integration time, and are typically between R 1000 and 3000.